Photon-induced near-field electron microscopy (PINEM): theoretical and experimental

2010 New J. Phys. 12 123028

(http://iopscience.iop.org/1367-2630/12/12/123028)

New Journal of Physics
The open-access journal for physics

Photon-induced near-field electron microscopy (PINEM): theoretical and experimental

Sang Tae Park, Milo Lin and Ahmed H Zewail[1]
Physical Biology Center for Ultrafast Science and Technology, Arthur Amos Noyes Laboratory of Chemical Physics, California Institute of Technology, Pasadena, CA 91125, USA
E-mail: zewail@caltech.edu

New Journal of Physics **12** (2010) 123028 (57pp)
Received 15 September 2010
Published 17 December 2010
Online at http://www.njp.org/
doi:10.1088/1367-2630/12/12/123028

Abstract. Electron imaging in space and time is achieved in microscopy with timed (near relativistic) electron packets of picometer wavelength coincident with light pulses of femtosecond duration. The photons (with an energy of a few electronvolts) are used to impulsively heat or excite the specimen so that the evolution of structures from their nonequilibrium state can be followed in real time. As such, and at relatively low fluences, there is no interaction between the electrons and the photons; certainly that is the case in vacuum because energy–momentum conservation is not possible. In the presence of nanostructures and at higher fluences, energy–momentum conservation is possible and the electron packet can either gain or lose light quanta. Recently, it was reported that, when only electrons with gained energy are filtered, near-field imaging enables the visualization of nanoscale particles and interfaces with enhanced contrast (Barwick *et al* 2009 *Nature* **462** 902). To explore a variety of applications, it is important to express, through analytical formulation, the key parameters involved in this photon-induced near-field electron microscopy (PINEM) and to predict the associated phenomena of, e.g., forty-photon absorption by the electron packet. In this paper, we give an account of the theoretical and experimental results of PINEM. In particular, the time-dependent quantum solution for ultrafast electron packets in the nanostructure scattered electromagnetic (near) field is solved in the high kinetic energy limit to obtain the evolution of the incident electron packet into a superposition of discrete momentum wavelets. The characteristic length and time scales of the halo of

[1] Author to whom any correspondence should be addressed.

electron–photon coupling are discussed in the framework of Rayleigh and Mie scatterings, providing the dependence of the PINEM effect on size, polarization, material and spatiotemporal localization. We also provide a simple classical description that is based on features of plasmonics. A major part of this paper is devoted to the comparisons between the theoretical results and the recently obtained experimental findings about the imaging of materials and biological systems.

Contents

1. Introduction

The recent development of photon-induced near-field electron microscopy (PINEM) [1, 2] has opened up new vistas for imaging with electrons. In the presence of matter, the unique interaction between electrons and photons results in the unraveling of the nanostructures involved. From the total population of transmitted electrons, PINEM can select for those electrons that have absorbed/emitted light quanta from nanoscale electromagnetic fields, allowing for the illumination of particles and boundaries between distinct media. Consequently, the spatial resolution of once-dark structural features can be imaged (‘lighted up’) on the

nanoscale and potentially reaching the atomic scale of electron microscopy [3]. Moreover, by capturing the evanescent field on its intrinsic time scale (femtoseconds), PINEM provides imaging in both space and time, and with orders of magnitude signal enhancement [4]–[6].

Apart from the promise of PINEM as a technique, the elucidation of the remarkable effect whereby tens of photons are absorbed/emitted *and* imaged by electrons is a significant objective in and of itself. We shall use PINEM interchangeably to mean the effect with 'M' being 'microscopic' and as the technique with 'M' being 'microscopy'. The PINEM effect can be understood by answering two distinct but related questions. Firstly, how can the electron absorb/emit any photons at all? Secondly, how can tens of photons be allowed? The diffraction of an electron beam by a standing electromagnetic wave was foreseen in 1933 by Kapitza and Dirac (the Kapitza–Dirac (KD) effect) [7], who showed that counter-propagating electromagnetic waves (a standing wave) can act as an effective diffraction grating. Depending on the focusing of the light beams, i.e. the angular uncertainty that gives rise to uncertainty in the spatial frequency or wave vector ($\vec{k}$) [8, 9], there result absorption and stimulated emission that give rise to diffraction restricted to net *even* quanta of momentum change. Direct experimental manifestations of the KD effect were reported by resolving the minute angles of reflection and related features [10]–[12].

However, without such a configuration, the net absorption/emission of photons by electrons in free space is forbidden due to energy–momentum conservation, as discussed below. Nevertheless, this energy–momentum mismatch can be eliminated by altering the dispersion relation of photons using matter [13, 14]. The phase velocity of light, which is the ratio of the angular frequency (ω) to the spatial frequency (k), can be slowed in a dielectric material, allowing for matching through k (see below). One example for changing the phase velocity is to propagate light in a dielectric gas, as in the known inverse Cerenkov effect [15]. Similarly, in the inverse Smith–Purcell effect [16], the amplitude/phase modulation of near-field light scattered from a grating can induce momentum shifts and lead to absorption/emission of photons by electrons. In the case of PINEM, the nanomaterial to be imaged plays the critical role of energy–momentum matching, with energy exchange in tens of electronvolts, which can easily be resolved in the energy spectra. The spatial confinement gives rise to momentum spread [17] and hence the matching. The temporal resolution enables the maximum field to be captured and utilized in imaging.

Figure 1 (top) illustrates the energy–momentum matching condition by means of energy or momentum spread. The green line represents the dispersion relation for a free photon in vacuum, whereas the blue dotted line represents the momentum change needed for a 200 keV electron to match the photon at the energies indicated. In free space, as marked, the two lines do not overlap and hence the interaction is not allowed. However, a significant energy spread due to temporal confinement (vertical ellipse) or momentum spread due to spatial confinement (horizontal ellipses) can allow for such interaction. For PINEM, at a given photon energy, the longitudinal momentum must spread by a large amount in order to allow for net photon absorption/emission (inelastic process) with acceleration and deceleration. On the other hand, in the KD effect, the net energy change (absorption/stimulated emission) is zero, resulting in an elastic process that leads to a minute angle change; the change in longitudinal momentum is small (see blue/red vectors in figure 1 (top) inset) and easily matched by laser-focusing confinement. We note that ultrafast PINEM leads to energy uncertainty that is relatively small, as indicated by the width of the 'pancake,' but it is possible on the attosecond scale to utilize the $\Delta t\,\Delta\omega$ uncertainty for matching, as discussed later.

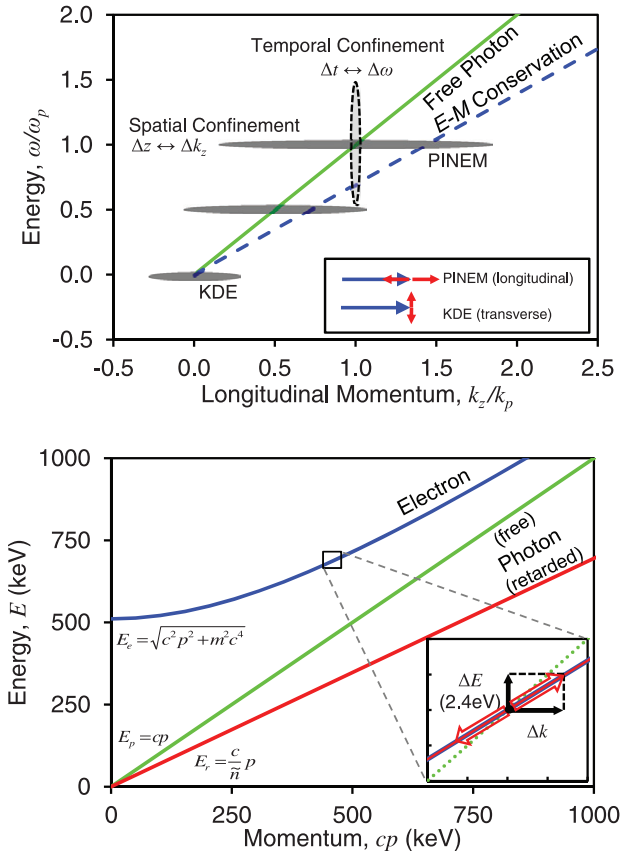

Figure 1. Energy–momentum conservation and the uncertainty in time and space. (Top) energy–momentum conservation of free electron and free photon via momentum broadening (horizontal ellipses) due to spatial confinement and energy broadening (vertical ellipse) due to temporal confinement. The solid green line represents the dispersion relation of a free photon, and the dotted blue line represents the momentum change of a free electron at the given energy change. For PINEM, the electron changes its energy by a single-photon quantum and its momentum by a value larger than that of a free photon of the same energy. For the KD effect, the electron energy is unchanged, whereas the transverse momentum is changed by two quanta of photon momentum, and the longitudinal momentum is virtually unchanged (see the inset). (Bottom) The relativistic dispersion relation of an electron (solid blue line), a free photon (solid green line) and a retarded photon (solid red line). (Bottom inset) Changes of momentum and energy of an electron and a photon. The energy change of 2.4 eV (black vertical arrow) of the retarded photon (red arrow) and corresponding momentum change (black horizontal arrow) must overlap with those of the electron (blue).

The energy–momentum conservation is necessary but not sufficient for coupling. This is because the component of the electric field in the direction of electron propagation (longitudinal direction) must be nonzero to accelerate or decelerate the electrons. The degree of photon absorption/emission in PINEM must therefore depend on the strength of the coupling and the orientation between the photon electric field and electron propagation. However, one has

to ask the question raised earlier: How can the electron absorb/emit so many photons, up to eight [1] or many tens for silver nanowire, as discussed below? And what is the nature of the process, coherent or incoherent? The interaction of thermally excited phonons with electrons has been reported by Boersch *et al* [18]; the energy loss/gain is meV for phonons and their resolution in the energy spectra is limited because of the near-eV spectral broadening. The potential of photon interaction to widen the energy spectra has been explored by Howie [19] in relation to STEM and other detections. In their theoretical treatment of the interaction of electrons with evanescent fields, García de Abajo and co-workers derived the probabilities of single [20] and multiple [21] absorption/emission. For the case of multiple events, they considered the solution to the Lippman–Schwinger equation in powers of interaction and propagation, with the corresponding coefficients in the expansion recursively and numerically obtained.

In this paper, armed with scattering theory, we show how the scattering approach provides an intuitive picture that is predictive of the key parameters involved in PINEM imaging of different finite-sized objects. We first consider the solution of the scattered partial waves in the Rayleigh and Mie regimes and then allow the field to interact with incident electrons at different impact parameters. Instead of using the perturbative expansion method, we solve the time-dependent Schrödinger equation analytically, in the PINEM regime, providing directly the relevant PINEM field, which satisfies energy–momentum conservation when coupled to the electron, and its dependence on spatial, energy, polarization and temporal characteristics. We shall compare the results obtained with those of multiple photon absorption/emission kinetics and time-integrated transition probabilities [22]. A major part of this paper is devoted to the comparisons of the theoretical results with the experimental findings obtained using PINEM imaging of nanomaterials and biological systems.

Before presenting these theoretical and experimental results, we discuss in what follows considerations of energy–momentum conservation and the evanescent fields of plasmonics, which are characteristic of metals and metal-like materials. The scattering theory approach is not limited to metals and here we apply it to both metallic and dielectric structures.

2. Energy–momentum conservation

Consider the interaction of an electron and a photon that are propagating with an angle Θ relative to each other. The relativistic electron energy is given by

$$E_e = \sqrt{c^2 p_e^2 + m_e^2 c^4}, \tag{1}$$

where m_e, p_e and E_e are the electron mass, momentum and energy, respectively. The photon momentum in the direction of the electron is $p_{//} = \hbar k_p \cos\Theta$ and the one perpendicular to it is $p_\perp = \hbar k_p \sin\Theta$, where k_p is the photon spatial frequency (wave vector). Because the total energy is $\sqrt{c^2(p_{//}^2 + p_\perp^2) + m_e^2 c^4}$, in order to absorb the photon, the electron must gain energy and momentum compatible with its relativistic dispersion relation,

$$E_e + \hbar\omega_p = \sqrt{c^2(p_e + \hbar k_p \cos\Theta_c)^2 + c^2(\hbar k_p \sin\Theta_c)^2 + m_e^2 c^4}, \tag{2}$$

where the photon angular frequency is given by ω_p. The critical angle Θ_c is defined such that equation (2) can be satisfied. Solving equation (2) for the critical angle,

$$\cos\Theta_c = \frac{2\hbar\omega_p E_e + (\hbar\omega_p)^2 - (\hbar k_p c)^2}{2\hbar k_p c^2 p_e} \approx \frac{\omega_p E_e}{k_p c^2 p_e}. \tag{3}$$

In the approximate limit described in equation (3), we take advantage of the fact that the electron energy is five orders of magnitude greater than the photon energy ($E_e \gg \hbar\omega_p \approx \hbar k_p c$), which is the case in PINEM experiments. Noting that the group velocity of the electron is $v_e = (\partial E_e/\partial p_e) = (c^2 p_e/E_e)$ and that the phase velocity of the photon is $\bar{v}_p = (\omega_p/k_p)$, equation (3) becomes

$$\frac{\bar{v}_p}{v_e} = \cos\Theta_c \leqslant 1. \tag{4}$$

In equation (4), conservation of energy and momentum has been reduced (in the high electron energy limit) to the matching of the photon phase velocity and the electron group velocity. It follows that in vacuum, when $\omega_p/k_p = c$, photon absorption/emission by an electron is not possible because v_e cannot equal or exceed c. For coupling to occur, the phase velocity of the photon must be lowered from c to at most the velocity of the electron, and this is accomplished through the variation of k_p via the material (e.g. in the inverse Cerenkov effect). This is graphically illustrated in figure 1 (bottom), in which the phase velocity of light must be decreased to match the slope (group velocity) of the electron dispersion curve. Another important consequence of equation (4) is that the equality is descriptive of the Θ dependence and thus the velocity matching can be reached by having an appropriate angle as well as a dielectric structure to decrease the phase velocity of light. It is to be noted that the condition in equation (4) is necessary but not sufficient for effective electron–photon coupling; the strength of the interaction depends on the magnitude of the electric field in the direction of electron propagation, as mentioned above and discussed below.

To investigate the mechanism by which the photon phase velocity is slowed by a metal plasmon, we will consider the dielectric function, which is necessary for the calculation of the dispersion relation. The relationship between resonant absorption and the refractive index of a material is well known, especially for a simple model of an atom with a single electron bound by a harmonic potential and acted upon by the external electric field (see for example [23]–[25]). Here, we only highlight the basic features that will be used later to compare with the results of scattering theory. In this picture, the equation of motion for the electron corresponds to that of a forced, damped harmonic oscillator, $m_e\ddot{z} + m_e\gamma\dot{z} + m_e\omega_0^2 z = -eE$, where z is the charge displacement distance, m_e and $-e$ are the electron mass and charge, ω_0 is the frequency of the harmonic potential, γ is a phenomenological damping (friction) coefficient, and E is the electric field. If the electric field varies sinusoidally in time as $E_0 e^{-i\omega t}$, then the solution reduces to $z = eE(m_e\omega^2 + im_e\gamma\omega - m_e\omega_0^2)^{-1}$.

The electric displacement $D = \varepsilon_0 E + P$ is due to both the external field E and the induced polarization, $P = -Nez$, in the material, where ε_0 is the permittivity of free space and N is the number density. Combining these relations, one obtains

$$D \equiv \varepsilon_0\varepsilon(\omega)E = \varepsilon_0\left(1 - \frac{Ne^2/m_e\varepsilon_0}{\omega^2 - \omega_0^2 + i\gamma\omega}\right)E,$$

where $\varepsilon(\omega)$ is the frequency-dependent dielectric function. For the case of a metal, the electron is assumed to be free, and in this case the restoring force vanishes ($\omega_0 = 0$), yielding the following dielectric function,

$$\varepsilon(\omega) = 1 - \frac{\omega_{\mathrm{bp}}^2}{\omega^2 + \mathrm{i}\gamma\omega}, \tag{5}$$

where $\omega_{\mathrm{bp}} = (\mathrm{N}e^2/m_e\varepsilon_0)$ is the bulk plasma frequency. Equation (5) gives the dielectric function of an ideal conductor as a function of the external field frequency, which is known as the classic Drude model solution [25]. For noble metals, electrons outside of the conduction band also contribute to the dielectric function, yielding the empirically corrected dielectric function, $\varepsilon(\omega) = \varepsilon_\infty - (\omega_{\mathrm{bp}}^2/\omega^2 + \mathrm{i}\gamma\omega)$, where $\varepsilon_\infty = 1$ for an ideal conductor in which no electrons are bound [26]. The dielectric function is important in determining the properties of evanescent plasmon waves, and below we consider its relevance to electron imaging.

3. Photon-induced near-field electron microscopy (PINEM) and evanescent plasmonics: the simple, particle picture

Here, before discussing the PINEM results using the quantum formalism and scattering theory, it is useful to consider the simple (classical) approach of plasmonics for which evanescent wave modes at the interface 'inherit' the refractive index of the material and hence the velocity matching needed for the coupling. For this reason, in this section we shall deal with two different cases: the case of a planar material with one characteristic mode and the case of a cylinder for which many modes exit; for the latter case, the existence of many modes and the surface curvature allow for the matching condition to be satisfied, unlike the planar case. The process is assumed to be a collision between an electron and a photon at a single point in space. The particle picture is therefore limited and does not provide the quantitative result of the scattering theory–time-dependent Schrödinger equation approach presented in section 4.

3.1. Planar material

From the above, it is clear that electrons can only absorb/emit photons with phase velocity below c. On a planar surface such electromagnetic waves can indeed propagate at the interface between a metal and a dielectric. In figure 2 (top inset), this boundary is taken to be perpendicular to $\hat{z}$, the propagation direction, and we shall call the $x < 0$ and $x > 0$ regions material 1 (metal) and material 2 (dielectric), respectively. Considering a metal surface mode in the infinite planar geometry, the transverse-magnetic (TM) mode solution of Maxwell's equations above ($x > 0$) and below ($x < 0$) the boundary is the only nonzero solution for this geometry [25]. The magnetic field points in the $\hat{y}$-direction transverse to the direction of propagation ($\hat{z}$), but the electric field has both a transverse ($\hat{x}$) and a longitudinal ($\hat{z}$) component, namely

$$H_y = -A\mathrm{e}^{\pm k_{mx}x}\mathrm{e}^{\mathrm{i}k_z z}, \tag{6a}$$

$$E_x = -\frac{Ak_z}{\omega\varepsilon_0\varepsilon_m}\mathrm{e}^{\pm k_{mx}x}\mathrm{e}^{\mathrm{i}k_z z}, \tag{6b}$$

$$E_z = \mp\frac{\mathrm{i}Ak_{mx}}{\omega\varepsilon_0\varepsilon_m}\mathrm{e}^{\pm k_{mx}x}\mathrm{e}^{\mathrm{i}k_z z}, \tag{6c}$$

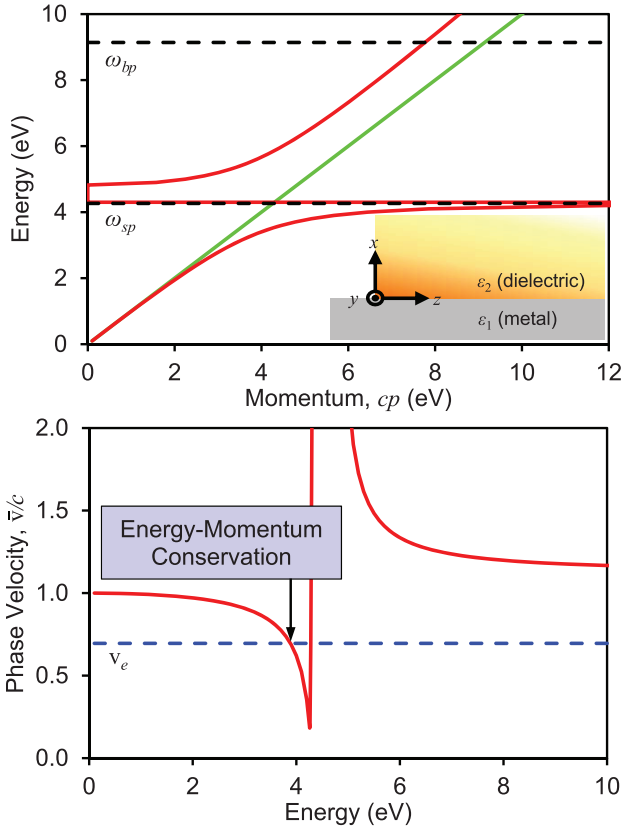

Figure 2. Dispersion relations of flat-surface plasmons. (Top inset) Schematic diagram of the boundary between dielectric (region 2) and metal (region 1). (Top) The dispersion curve based on the empirically corrected Drude model neglecting the friction is plotted for silver (red), along with the free photon (green). The bulk (ω_{bp}) and surface (ω_{sp}) plasmon frequencies are shown as dotted lines. (Bottom) The phase velocity as a function of the surface plasmon frequency. The group velocity of 200 keV electrons is shown as a straight line, with the intersection being the critical plasmon frequency at which absorption of the surface plasmon is permitted.

where the top sign refers to the region $m = 1$ ($x < 0$), the bottom sign refers to the region $m = 2$ ($x > 0$), and A is an amplitude coefficient. The TM wave equation is expressed as

$$\frac{\partial^2 H_y}{\partial z^2} + \left(\left(\frac{\omega}{c} \right)^2 \varepsilon - k_z^2 \right) H_y = 0. \tag{7}$$

Continuity of the electric field at the boundary implies that equation (6*c*) is the same for $m = 1$ and $m = 2$ at the boundary $x = 0$, thereby obtaining $(k_1 x/\varepsilon_1) + (k_2 x/\varepsilon_2) = 0$. Similarly, by plugging equation (6*a*) into the wave equation, equation (7), one obtains the additional relations $k_{mx}^2 + (\omega/c)^2 \varepsilon_m - k_z^2 = 0$. Finally, combining these relationships, one obtains expressions for the different components of the spatial frequency,

$$k_z = \frac{\omega}{c} \sqrt{\frac{\varepsilon_1 \varepsilon_2}{\varepsilon_1 + \varepsilon_2}}, \quad k_{mx} = \frac{\omega}{c} \sqrt{\frac{-\varepsilon_m^2}{\varepsilon_1 + \varepsilon_2}}. \tag{8}$$

Since regions 2 and 1 are dielectric and metal, respectively, $\varepsilon_2 = 1$ (for vacuum) and ε_1 is the metallic dielectric function (see the Drude model in the previous section); recall that $\varepsilon_1 \ll 0$ for metals. Finally, using equation (8), the phase velocity of this electromagnetic wave along the interface can be expressed as

$$\bar{v}_\mathrm{p} = \frac{\omega}{\mathrm{Re}[k_z]} \approx c\sqrt{\frac{\omega_\mathrm{bp}^2 - (\varepsilon_\infty + 1)\omega^2}{\omega_\mathrm{bp}^2 - \varepsilon_\infty \omega^2}}. \tag{9}$$

To see whether this phase velocity can be significantly lower than c, the rhs of equation (9) has been simplified in the negligible friction limit (i.e. $\gamma \ll \omega$), which holds for metals [25]. As $\omega \to \omega_\mathrm{bp}/\sqrt{\varepsilon_\infty + 1} \equiv \omega_\mathrm{sp}$, the phase velocity $\bar{v}_\mathrm{p} \to 0$, where ω_sp is the surface plasmon frequency (see figure 2 (top)). Therefore, only for a limited range of frequencies (from 3.9 eV to 4.3 eV) the phase velocity of the surface wave can be reduced to match any velocity the electron may have. If k_z were purely real, then from equation (6) there would be undamped propagation in the z-direction. However, as can be seen from equation (5), the presence of a nonzero friction coefficient γ introduces an imaginary component, $k_z = \mathrm{Re}[k_z] + \mathrm{i}\,\mathrm{Im}[k_z]$. Therefore, the propagation factor in the z-direction becomes $\exp(\mathrm{i}\,k_z z) = \exp(\mathrm{i}\,\mathrm{Re}[k_z]z)\exp(-\mathrm{Im}[k_z]z)$, which means that there exists a well-defined attenuation length, L_z. Likewise, in the transverse (x)-direction, the propagation of the wave in the dielectric (region 2) is $\exp(-k_{2x}x) = \exp(-\mathrm{Re}[k_{2x}]x)\exp(-\mathrm{i}\,\mathrm{Im}[k_{2x}]x)$, and the attenuation length in the x-direction is L_{2x}. These lengths are given by

$$L_z = \{\mathrm{Im}[k_z]\}^{-1}, \quad L_{2x} = \{\mathrm{Re}[k_{2x}]\}^{-1}. \tag{10}$$

By substituting the spatial frequencies (equation (8)) into equation (10), the attenuation lengths can be found as a function of ω for a metal with a given ω_bp, ε_∞ and γ. For example, using those parameters for silver, at $\hbar\omega_\mathrm{p} = 2.4$ eV excitation (off-resonant to the $\sim$4 eV surface plasmon resonance), we find that $L_{2x} = 260$ nm and $L_z = 8\,\mu$m. Thus, the wave extends along the surface and decays into the dielectric (and also into the metal).

In figure 2 (bottom), the phase velocity of the TM mode (equation (9)) is plotted as a function of incident photon frequency for TM evanescent waves on a planar silver surface, with the dielectric function obtained via fitting [26] of the Drude model to the experimental data [27]. The group velocity of our 200 keV electron is shown as a straight line. If the electron co-propagates with the photon, $\Theta_\mathrm{c} = 0$, and from equation (4) the photon phase velocity must match the electron velocity. Velocity matching occurs at 3.8 eV photon energy. Thus, based on conservation of energy and momentum, 2.4 eV photons cannot be absorbed or emitted by 200 keV electrons at an infinite planar surface, which exhibits the single mode of equation (6). Moreover, for photon energies greater than 3.8 eV, absorption by the electron would only be possible by fine-tuning the electron–photon angle Θ (corresponding to an electron incident angle of $\pi/2 - \Theta$ relative to the flat metal surface), in which the required fine-tuning precision depends on the momentum spread of the evanescent photon.

Within the plasmonics treatment, these limitations can be overcome when a structure with nanoscale dimension(s) (e.g. a cylinder) is employed such that there are multiple modes with radius-dependent dispersion that allow for such matching.

3.2. Cylindrical material

Consider a cylinder of radius a, with r and y corresponding to the radial and axial directions (see figure 3 (top)). A surface wave can travel angularly (along θ) as well as axially

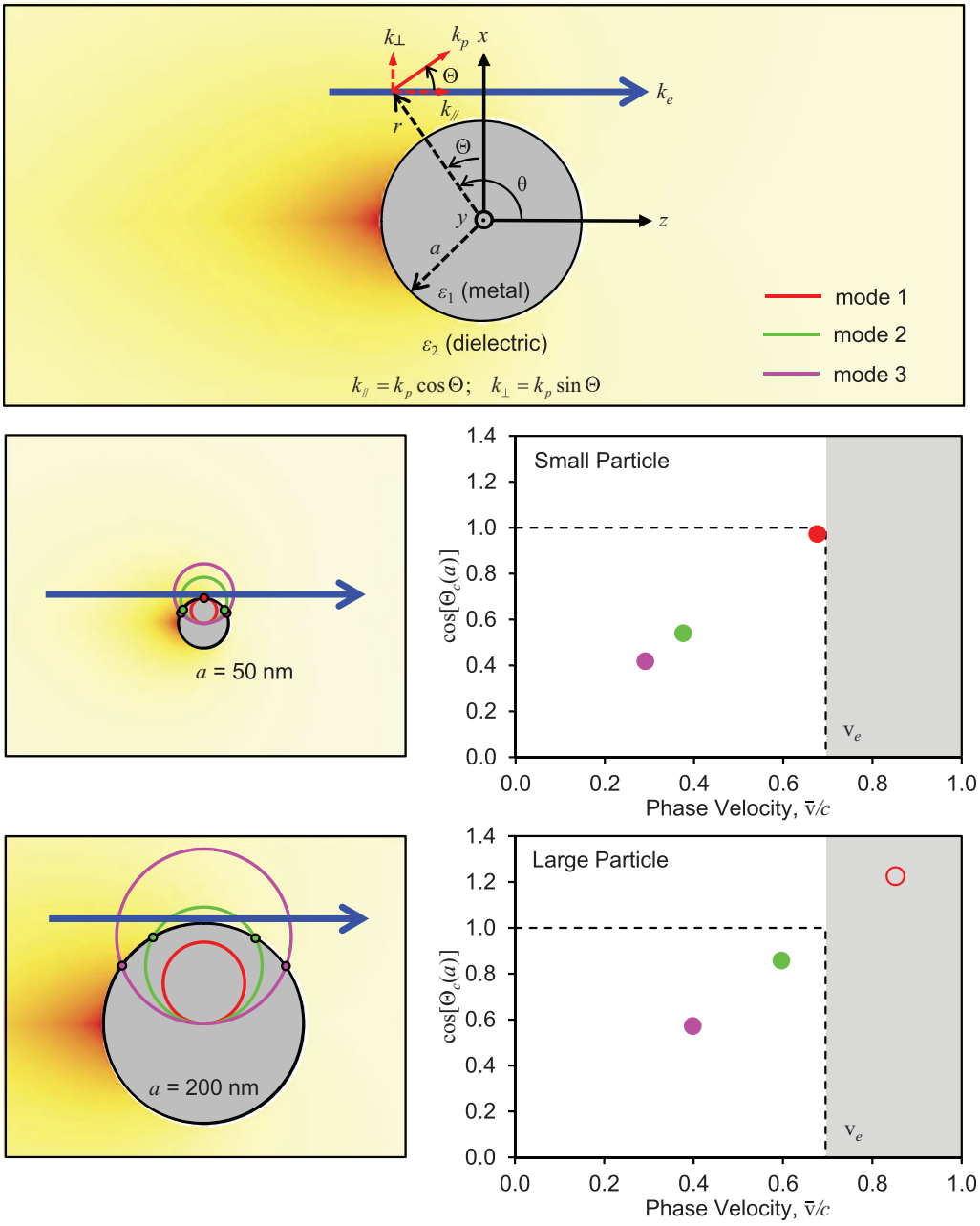

Figure 3. Electron–plasmon interaction. (Top) Schematic geometry of cylindrical surface plasmon and free electron. The halo of evanescent modes is drawn for visualization purposes, assuming that cylindrical modes start from $\theta = \pi$, where the incident wave hits first, and propagate in both directions. For 200 keV electrons and 2.4 eV photons, the tangential phase velocities and critical angles at the cylinder surface (right) for the first three modes are shown for silver nanowires of (middle) 50 nm and (bottom) 200 nm radii. The left panels show the 'interaction cross sections' (see text) of electron–photon coupling.

(along y), resulting in helical propagation along the cylinder. Solving Maxwell's equations in this geometry for purely angular motion (no axial propagation), the electric field components of the pure angular mode propagating in vacuum outside the cylinder are [28]

$$E_r = Z_r(r)\exp[\mathrm{i}(\beta\theta - \omega t)]; \quad E_\theta = Z_\theta(r)\exp[\mathrm{i}(\beta\theta - \omega t)]. \tag{11}$$

In equation (11), $Z_r(\mathrm{r}) = -A_\beta\beta(k_\mathrm{p}r)^{-1}H_\beta(k_\mathrm{p}r)$ and $Z_\theta(\mathrm{r}) = \mathrm{i}A_\beta H'_\beta(k_\mathrm{p}r)$, where $k_\mathrm{p} \equiv \omega/c$, $H_\beta(x)$ is the Hankel function of the first kind of order β [29, 30]; A_β are amplitude coefficients, and differentiation is taken with respect to the argument.

As can be seen from equation (11), the wave solution travels tangentially with spatial frequency β/r. By applying the boundary conditions that the tangential components of the electric field and the magnetic field must be continuous at the surface, the following condition is obtained [31],

$$\varepsilon_1 = \frac{J'_\beta(\sqrt{\varepsilon_1}k_\mathrm{p}a)H_\beta(k_\mathrm{p}a)}{J_\beta(\sqrt{\varepsilon_1}k_\mathrm{p}a)H'_\beta(k_\mathrm{p}a)}.$$

For a given $\omega = k_\mathrm{p}c$, there are an infinite number of complex tangential angular frequencies β that satisfy this equation and can be numerically solved. Each solution corresponds to a different mode with tangential phase velocity in the angular direction, $\bar{v}_\mathrm{p} = \omega\{\mathrm{Re}[\beta/r]\}^{-1}$. Therefore, the energy–momentum matching condition (equation (4)) is expressed as

$$\cos[\Theta_\mathrm{c}(r)] = \frac{\omega}{v_\mathrm{e}\,\mathrm{Re}[\beta/r]} = \left(\frac{r}{a}\right)\cos[\Theta_\mathrm{c}(a)], \tag{12}$$

where $\Theta_\mathrm{c}(r)$ is the critical angle as a function of the distance, r, from the center of the cylinder and $\Theta_\mathrm{c}(a)$ is the critical angle at the surface of the cylinder. Since the electron and the angular modes propagate in $\hat{z}$ and $\hat{\theta}$, respectively, the angle between the two is $\Theta = \theta - \pi/2$ (see figure 3 (top)).

For each mode, equation (12) defines an 'interaction cross section', given by the polar coordinates $(r,\ \Theta_\mathrm{c}(r))$ for all y along the cylinder axis, which traces a curved plane in space; each point on that plane is a position at which the electron can absorb/emit the photon while conserving energy and momentum. An electron with group velocity v_e can couple to the mode as it passes through this plane. This velocity matching procedure is akin to the inverse Cerenkov effect [15], except that velocity matching for the cylindrical mode is satisfied at an 'interaction point' using the instantaneous phase velocity, rather than along the entire electron trajectory using a uniform phase velocity. Note that the dispersion relation is altered inside the dielectric medium for the inverse Cerenkov effect, while the dielectric function of the metal cylinder alters the near-field dispersion in vacuum outside the cylinder; in this respect, the plasmonic picture is similar to the inverse Smith–Purcell effect [16] whereby the grating induces near-field amplitude/phase modulation, leading to discrete shifts of the photon momentum in vacuum and hence coupling.

For the β of each mode, the tangential spatial frequency β/r decreases away from the cylinder center. Thus, as can be seen in equation (12), the critical angle also decreases with increasing r. There is a maximum radius r_MAX, such that $\Theta_\mathrm{c}(r_\mathrm{MAX}) = 0$, and electron–photon coupling cannot occur for $r > r_\mathrm{MAX}$. From equation (12) we obtain $r_\mathrm{MAX} = (a/\cos[\Theta_\mathrm{c}(a)])$.

Therefore, there is a well-defined cut-off length L_β (from the surface) within which electron–photon coupling can occur. This length is given by

$$L_\beta = r_{\mathrm{MAX}} - a = \left(\frac{1}{\cos\left[\Theta_{\mathrm{c}}(a)\right]} - 1\right) a. \tag{13}$$

Higher-order modes have larger tangential spatial frequencies and therefore longer cut-off distances.

Consider the interaction of an electron with the tangential modes of a cylinder discussed above. For the first three modes, the middle and bottom panels of figure 3 show the critical angles for which the phase velocity matches the electron velocity for 200 keV electrons and 2.4 eV photons incident on silver nanowires with two different wire radii. The higher-order modes have increasing values of Im[β], which correspond to faster tangential decay and hence the diminished overlap with the imaging electron. For each wire size, the right panel shows $\cos[\Theta_{\mathrm{c}}(a)]$ for each mode, whereas the left panel displays the 'interaction cross section' of the modes as given by equation (12); from equation (13), the spatial extent of the cross section outside of the cylinder is given by L_β.

There are two important differences between the cylindrical and planar situations. Firstly, the existence of multiple modes with decreasing tangential phase velocity allows for the existence of mode(s) with phase velocity below the electron velocity, in contrast to the planar case for which there exists only a single mode that may or may not have a phase velocity below the electron velocity. Secondly, for modes with phase velocity below the electron velocity, the curvature of the cylindrical surface means that, as the wave travels over the surface, it will pass through the 'interaction plane', which satisfies equation (12), such that the electron can couple to the mode while conserving energy and momentum.

The picture presented above for a metal plasmon gives a simple illustrative description of the PINEM phenomenon as a classical, point interaction between electrons and photons. It is important to note that because the scattered wave is confined (i.e. radially decaying spherical or cylindrical wavelets), the electric field experienced by the traveling electron decomposes into a distribution of spatial frequency components. Therefore, it is necessary to calculate the full pattern of the scattered fields and employ the quantum mechanical formalism, which considers electron–photon coupling as a *wave* evolution, in order to ascertain all of the components of the scattered light that can couple with the electron; this is the focus in what follows.

4. PINEM: theoretical

In this section, we consider the formal mathematical solution of the PINEM effect: first the scattering of light from a nanostructure in the Mie and Rayleigh regimes and then the influence of this scattered light on imaging with electrons by solving the time-dependent Schrödinger equation. Throughout the paper, we shall designate this approach as the scattering-of-photon/time-dependent Schrödinger equation (STS). The results are compared with the experimental findings. In appendices A and B, we shall give the details of the mathematical solutions.

As shown in appendix B, the solution for scattering from an object of comparable size to λ are complicated because they involve an infinite summation of spherical (e.g. particle) or cylindrical (e.g. nanowire) wavelets. In order to elucidate the physics of the scattering process,

we will discuss first the Rayleigh (dipole) limit for spheres, which is valid for nanoparticles whose dimensions are significantly smaller than the wavelength of incident light. This allows us to develop features of scattering for the small radius limit, which would be obscured by the mathematical machinery of the general (Mie) solution.

The electric field of the incident light acting on a particle creates a temporally oscillating polarization, which in turn radiates electromagnetic waves [23]. In the small-particle limit, the polarization of the particle can be thought of as a single oscillating dipole moment; classically, the charges are separated within the radiation cycle because of the relatively small dimensions of the object [32]. For light with angular frequency ω, the induced dipole moment, $\vec{\mu}$, is

$$\vec{\mu} = 4\pi\varepsilon_0\chi_s a^3 \vec{E}_0 \exp[-\mathrm{i}\omega t], \tag{14}$$

where $\tilde{n}$ is the (complex) refractive index of the material, a the radius of the particle and ε_0 the vacuum permittivity; χ_s, the spherical susceptibility, is given by $\chi_s = (\tilde{n}^2 - 1)(\tilde{n}^2 + 2)^{-1}$. The oscillating dipole moment, $\vec{\mu}$, generates an outwardly radiating electromagnetic field,

$$\tilde{E}(\vec{r}, t) = \frac{1}{4\pi\varepsilon_0 r^3}(k^2 r^2 \hat{r} \times \vec{\mu} \times \hat{r} + (1 - \mathrm{i}kr)\,(3\hat{r}(\hat{r} \cdot \vec{\mu}) - \vec{\mu}))\,\mathrm{e}^{\mathrm{i}kr}, \tag{15}$$

where k is the spatial frequency, r is the distance from the center of the particle and $\hat{r}$ is its unit vector. In the vicinity of the particle ($r \approx a$), the near-field limit, the kr term can be ignored in equation (15) because $r \approx a \ll k^{-1}$ in the (Rayleigh) dipole approximation. Expressing equation (15) in Cartesian coordinates yields the near-field dipole limit,

$$\begin{aligned} E_x(\vec{r}, t) &\approx E_0\chi_s\frac{a^3}{r^5}(2x^2 - y^2 - z^2)\mathrm{e}^{-\mathrm{i}\omega t}, \\ E_y(\vec{r}, t) &\approx E_0\chi_s\frac{a^3}{r^5}(3xy)\mathrm{e}^{-\mathrm{i}\omega t}, \\ E_z(\vec{r}, t) &\approx E_0\chi_s\frac{a^3}{r^5}(3zx)\mathrm{e}^{-\mathrm{i}\omega t}. \end{aligned} \tag{16}$$

In equation (16), we have chosen the incident electric field to be polarized in the $\hat{x}$-direction, such that $\vec{E}_0 = E_0\hat{x}$.

For a near-field point (see figure 4), which we shall invoke for the interaction with electrons, $x = b\cos\phi$, where ϕ is the azimuth angle with respect to the light polarization and b is the impact parameter. From the x-dependence of equation (16), we see that $E_z \propto \cos\phi$, as is the case for the (Mie) exact solution shown in appendix B. It is to be noted that the near-field components are fast-decaying (evanescent) with r^{-3} dependence. Close inspection of equation (16) reveals that the transverse field, E_x, has $1/\mathrm{e}$ depth of $\sim a/3$ along the x-direction and Gaussian σ-width of $\sim a/\sqrt{6}$ along the z-direction. The longitudinal field component, E_z, has $1/e$ depth of $\sim a/3$ along the x-direction.

A similar result holds for an infinite cylinder of small radius by taking the first-order term (thin wire approximation) of the general cylindrical solution (equation (B.2)). The resulting

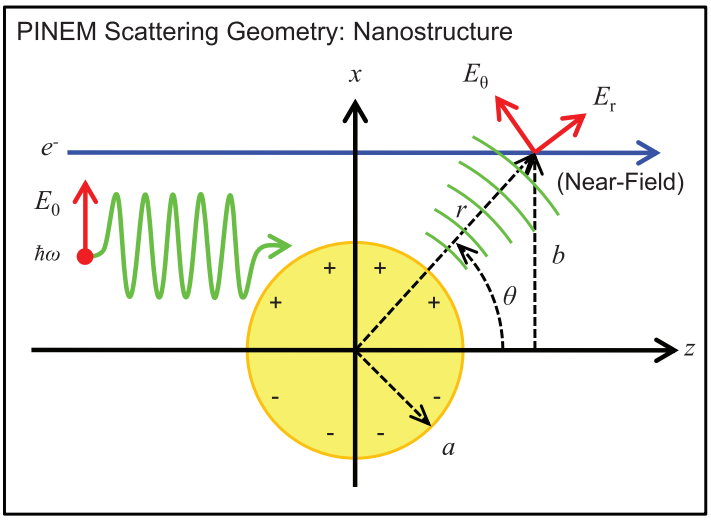

Figure 4. Schematic diagram of three-body interactions of PINEM. The electron, incident light and nanoparticle in spherical and cylindrical geometries are shown. a and b denote the radius of the particle and the impact parameter of the electron trajectory relative to the center of the particle, respectively. The electron and incident light both propagate in the $\hat{z}$-direction, and the polarization of the incident electric field is in the $\hat{x}$-direction. The symmetry axis in the cylindrical geometry is in the $\hat{y}$-direction. Note that for the incident electric field E_0, both possibilities for its direction are perpendicular to the shown electron propagation (no coupling), whereas the scattered field can couple.

electric fields in Cartesian coordinates are

$$\begin{aligned} E_z(\vec{r},t) &\approx E_0\chi_c\frac{a^2}{r^4}(2xz)\mathrm{e}^{-\mathrm{i}\omega t} \\ E_x(\vec{r},t) &\approx E_0\chi_c\frac{a^2}{r^4}(x^2-z^2)\mathrm{e}^{-\mathrm{i}\omega t} \\ E_y(\vec{r},t) &= 0, \end{aligned} \tag{17}$$

where $\chi_c = (\tilde{n}^2-1)(\tilde{n}^2+1)^{-1}$ is the cylindrical susceptibility. As in the spherical case, $\vec{E}_0 = E_0\hat{x}$, and the symmetry axis is along the y-direction. From equation (17), it follows that the transverse field, E_x, has $1/e$ depth of $\sim a/2$ along the x-direction and Gaussian σ-width of $\sim a/\sqrt{2}$ along the z-direction, whereas the longitudinal component, E_z, has $1/e$ depth also of $\sim a/2$ along the z-direction. For both spherical and cylindrical geometries in the small-particle scattering limit, we can understand the polarization dependence and characteristic skin depth of the scattered light, which are also descriptive of the exact scattering solutions [33] (see equations (B.1) and (B.2)) computed in this paper.

Knowing the electromagnetic field distribution adjacent to nanoparticles, we can now solve for the effect of this field on ultrafast electrons. The electron 'sees' evanescent photons in the near-field range. Figure 4 illustrates the geometry and in it we define the key parameters involved. We note that the incident photon in this case propagates with its electric field perpendicular to the electron trajectory (which in principle leads to no coupling, as discussed in

section 2), but the scattered spherical wave has a field component that allows for such coupling; if the incident electric field is perpendicular to the plane, the scattered wave will not allow for such a coupling; thus even for a spherical wave there is a polarization anisotropy.

The time evolution of the wavefunction of an electron traveling through the scattered electromagnetic wave can now be expressed in the PINEM regime where the electron kinetic energy is much larger than the interaction energy with the photon. A detailed derivation of the solution is given in appendix A. This type of quantum treatment of electron–photon interactions has been invoked in other studies of, e.g., high harmonics (i.e. interaction of 'bound' electron and free photon) [34]–[37], and includes the equivalent classical action (local phase) approach [36]. The wavefunction of the electron is defined in terms of the moving envelope function $g(z', t')$ and the carrier wave,

$$\Psi(z, t) = g(z - v_e t, t)\ \exp[\mathrm{i}(k_e z - \omega_e t)]. \tag{18}$$

The moving frame, $z' = z - v_e t$, is chosen to be at the group velocity, v_e, of the electron packet, such that z' is the relative position from the center of the packet. The envelope function in the moving frame coordinate carries the initial wave packet profile and the final phase change due to the interaction with the scattered wave.

For an electron in the presence of the electromagnetic field, the Hamiltonian, using the Coulomb gauge, can be written as

$$H = \frac{\hat{p}_e^2}{2m_e} + \left(\frac{e}{m_e}\right)\vec{A}\cdot\hat{p}_e + \frac{e^2A^2}{2m_e} \approx -\frac{\hbar^2\nabla^2}{2m_e} - \mathrm{i}\frac{e\hbar}{m_e}\frac{1}{2}\left(\frac{\tilde{E}}{+\mathrm{i}\omega_p} + \frac{\tilde{E}^*}{-\mathrm{i}\omega_p}\right)\cdot\vec{\nabla}, \tag{19}$$

where $\vec{A}$ is the vector potential and $\hat{p}_e$ is the momentum operator, with the second term being linear in the field whereas the third term is quadratically dependent (ponderomotive-type effect) (see appendix B). Because p_e is very large in PINEM, the second term $(\vec{A}\cdot\hat{p}_e)$ is dominant. In contrast, for the KD effect, $\vec{A}\cdot\hat{p}_e$ does not contribute (the A^2-term is dominant) because the transverse interaction has zero amplitude $(\hat{x}\cdot\tilde{E}_p = 0)$; the longitudinal interaction is momentum mismatched $(\Delta k_e^z \gg k_p$ and $k_p^z \approx 0)$ for an energy change of $\hbar\omega_p$. In equation (19), $\tilde{E}$ is the complex electric field; electrons can interact with the field of the scattered light, and either absorb (via the $\tilde{E}$ term) or emit (via the $\tilde{E}^*$ term) photon energy from (to) the field.

To consider pulsed radiation (with σ_p) and electron packets (with σ_e) of PINEM, we approximate the temporal intensity of the slowly varying $(\sigma_p \gg a/c)$ near-field scattered wave as a Gaussian function, and solve the time-dependent Schrödinger equation for the evolution of the wavefunction; for continuous-wave (CW) radiation, $\sigma_p \to \infty$. The final envelope function of the propagating electron (equation (18)) becomes (see appendix A for details)

$$g(z', +\infty) = g(z', -\infty)\exp\left[-\mathrm{i}\frac{e}{\hbar\omega_p}\left\{\exp\left[-\frac{(z' + v_e\tau)^2}{4v_e^2\sigma_p^2}\right]\right\}\left\{\mathrm{Im}\left(\exp\left[\mathrm{i}\frac{\omega_p}{v_e}z'\right]\tilde{F}_z\left(\frac{\omega_p}{v_e}\right)\right)\right\}\right]. \tag{20}$$

In equation (20), the component(s) of the electric field that couples to the electron, hereafter referred to as the 'PINEM field', is defined as

$$F_z\left(\frac{\omega_p}{v_e}\right) \equiv \int_{-\infty}^{+\infty} \mathrm{d}z''\, E_z(z'', 0)\exp\left[-\mathrm{i}\left(\frac{\omega_p}{v_e}\right)z''\right],$$

which is the (unnormalized) Fourier transform of the z-component (direction of propagation) of the scattered electric field at the spatial frequency $\Delta k_e = \omega_p/v_e$.

It follows that, for light with $k_p = \Delta k_e$, $\bar{v}_p = \omega_p/\Delta k_e = v_e$, which is precisely the condition for satisfying energy/momentum conservation for coupling of electron and photon, as predicted by equation (4). If there is no Fourier component of the electric field at this critical spatial frequency (i.e. $\tilde{F}_z(\omega_p/v_e) = 0$), then $g(z', t) = g(z', -\infty)$ in equation (20) and there is no interaction, because the wavefunction does not change. Moreover, if $E_z = 0$, then its Fourier transform $\tilde{F}_z$ is also zero, and again no interaction. Accordingly, for electron–photon coupling to occur, there must be a component of the electromagnetic wave with the appropriate phase velocity, and the component of the electric field that points in the direction of electron propagation must be nonzero, as was the case for the inverse Cerenkov effect discussed above.

A more transparent view of equation (20) can be obtained by the use of Taylor expansion and re-arrangement of the summation (the Jacobi–Anger relation [30]). Substituting the envelope function into the expression for the wavefunction (equation (18)), we obtain the final electron wavefunction,

$$\Psi(z, t \to +\infty) = g(z - v_e t, -\infty) \sum_{n=-\infty}^{\infty} \xi_n(z - v_e t) \exp\left[i \left(k_e + n\frac{\omega_p}{v_e} \right) z - i(\omega_e + n\omega_p)t \right], \qquad (21)$$

which displays both the spatial and the temporal features, with the coefficients defined by

$$\xi_n(z') \equiv \left(\frac{\tilde{F}_z}{|\tilde{F}_z|} \right)^n J_n \left(-\frac{e}{\hbar\omega_p} |\tilde{F}_z| \exp\left[-\frac{(z' + v_e\tau)^2}{4v_e^2\sigma_p^2} \right] \right),$$

where J_n is the Bessel function of the first kind of order n. In equation (21), the wavefunction decomposes into a sum of electron wavelets with discretely varying (evenly spaced) momenta with their envelope simply given by $g(z - v_e t, -\infty)\xi_n(z - v_e t)$.

4.1. Pulsed versus continuous-wave (CW) mode

For CW light and a continuous beam of electrons ($\sigma_p \to \infty$, $\sigma_e \to \infty$), the amplitudes of the momentum eigenstates in equation (21) become constants. In such a case, the wavefunction becomes a superposition of discrete spatial frequency components given by

$$\exp\left\{ i \left(k_e + \frac{n\omega_p}{v_e} \right) z - i(\omega_e + n\omega_p)t \right\},$$

with coefficients of $(\tilde{F}_z/|\tilde{F}_z|)^n J_n(-(e/\hbar\omega_p)|\tilde{F}_z|)$; the populations are therefore

$$\left\{ J_n \left(-\frac{e}{\hbar\omega_p} |\tilde{F}_z| \right) \right\}^2.$$

If the electron is pulsed ($\sigma_e < \infty$), the population becomes that of the nth state wave packet,

$$g\,(z - v_e t, -\infty) \exp\left\{ i \left(k_e + \frac{n\omega_p}{v_e} \right) z - i(\omega_e + n\omega_p)t \right\}.$$

On the other hand, for the PINEM experiments with pulsed light and electrons ($\sigma_p < \sigma_e < \infty$), the wavefunction (equation (21)) is a superposition of spatial frequency components, with the nth distribution centered at

$$\exp\left\{\mathrm{i}\left(k_e + \frac{n\omega_p}{v_e}\right)z - \mathrm{i}(\omega_e + n\omega_p)t\right\}.$$

The spread of each distribution in momentum space, especially the zeroth-order component, depends on the electron pulse length, the laser duration and the time delay (τ) between the two. The J_n term can be interpreted as a local probability density of the nth state, φ_n, as long as it is slowly varying compared to the light spatial frequency ($\omega_p\sigma_p \gg 1$). It follows that the probability of the nth state, $\langle\varphi_n|\Psi\rangle$, can be obtained by integrating over the nth envelope function,

$$P(n) = \int_{-\infty}^{+\infty} \mathrm{d}z' \left| g(z', -\infty) J_n\left(-\frac{e}{\hbar\omega_p}|\tilde{F}_z| \exp\left[-\frac{(z' + v_e\tau)^2}{4v_e^2\sigma_p^2}\right]\right)\right|^2. \tag{22}$$

Because $|J_{-n}(x)|^2 = |J_n(x)|^2$, we immediately see from equation (22) that $P(-n) = P(n)$; that is, the probability of net photon absorption is equal to that of net photon emission. The appearance of the Bessel function is reflective of the multiple pathways involved in electron–photon interactions, in this case of absorption and emission.

By inverse Fourier transformation of the final envelope function (equation (A.14)) and by integrating the square of the amplitude of the wavefunction in momentum space, we obtain $P(n)$ as a double summation,

$$P(n) = \sum_{j=0}^{\infty}\sum_{k=0}^{\infty} C_j^n C_k^{n^*} \left(1 + S_{njk}R_\sigma^2\right)^{-1/2} \exp\left[-\frac{S_{njk}R_\tau^2}{2\left(1 + S_{njk}R_\sigma^2\right)}\right], \tag{23a}$$

$$C_j^n = \frac{1}{(|n| + j)!\,j!}\left(\frac{e\tilde{F}_z}{2\hbar\omega_p}\right)^{n+j}\left(-\frac{e\tilde{F}_z^*}{2\hbar\omega_p}\right)^{j}, \tag{23b}$$

where $S_{njk} = n + j + k$, $R_\sigma = \sigma_e/\sigma_p$ and $R_\tau = \tau/\sigma_p$. The importance of equation (23) is in providing an analytical expression of the coupling coefficients in terms of the relevant parameters; apart from some definitions, the general form is consistent with equation (10) of [21], except that in [21] the coefficients are obtained numerically and recursively, and here we provide the C_j^n analytically. Equation (23) elucidates the importance of polarization anisotropy as well as the spatial and temporal localization, as discussed below.

4.2. PINEM field: analytical solution

To elucidate the physics of PINEM, we evaluate the PINEM field, $\tilde{F}_z$, analytically using the longitudinal component, E_z, for spherical (equation (16)) and cylindrical (equation (17)) geometries in the dipole limit, giving

$$|\tilde{F}_z| = |(E_0\cos\phi)\chi_s\, 2a^3\Delta k_e^2\{K_1(\Delta k_e b)\}| \quad \text{(sphere)}, \tag{24a}$$

$$|\tilde{F}_z| = |(E_0\cos\phi)\,\chi_c\,\pi\,a^2\Delta k_e \exp[-\Delta k_e b]\,| \quad \text{(cylinder)}, \tag{24b}$$

where the polarization dependence is expressed by the azimuth angle, ϕ, and the phase matching is described by $\Delta k_e^2 K_1(\Delta k_e b)$ for the sphere and by $\Delta k_e \exp[-\Delta k_e b]$ for the cylinder; both are determined by the impact parameter b and the change of electron momentum Δk_e, consistent with the conservation requirement. χ_s and χ_c are the susceptibilities defined above. For the CW case, the population expressed in [22] (equation (68)) is consistent with the expression for $\tilde{F}_z$ in equation (24*a*). At very small b (and a as well), the PINEM field for the two geometries simplifies to

$$|\tilde{F}_z| \approx \left| E_0 \cos\phi \chi_s \left(\frac{a^3}{b}\right) 2\Delta k_e \right| \quad \text{(sphere)}, \tag{25a}$$

$$|\tilde{F}_z| \approx \left| E_0 \cos\phi \chi_c \frac{a^2}{1+\Delta k_e b} \pi\ \Delta k_e \right| \quad \text{(cylinder)}, \tag{25b}$$

which is proportional to a cross-sectional area a^2 (the size effect), and the matching is simply given by $\Delta k_e \equiv \omega_p / v_e$ (no Bessel functions!). We note that the matching criterion is now evident from the scattering theory approach and is consistent with the classical picture given in figure 1: $\Delta\omega_e / \Delta k_e = v_e$, $\Delta k_e = k_e^{(f)} - k_e^{(i)}$, $k_p = \omega_p / \bar{v}_p$ and hence $\Delta k_e = n k_p (\bar{v}_p / v_e)$ for $\Delta\omega_e = n\omega_p$; only when $\bar{v}_p = v_e$ would n photon absorption and emission be conserved through Δk_e.

The above treatment is for the case of $a \ll \lambda$. As a approaches λ, we must obtain the exact solution for the electromagnetic fields and their interactions with the electron. For the spherical geometry, the incident wave is decomposed into a superposition of spherical wave solutions and matched to the internal and the scattered waves consistent with the polarization of the material. Such a solution was obtained by Mie for a sphere of arbitrary size [38]. The (Mie) exact solution used in our calculations of photon scattering is well described in the literature [33, 39, 40], and for computation purposes we invoke the equations given in appendix B.

4.3. PINEM field amplitudes

It has been shown (see appendix A for details) that it is the longitudinal component of the field (E_z) that couples with electrons and that the probability of transition depends on the PINEM field, $\tilde{F}_z(\omega_p / v_e)$, which is the Fourier component of the electric field, E_z, at the spatial frequency of $\Delta k_e = \omega_p / v_e$. Therefore, the calculation of these two quantities is at the heart of understanding the PINEM effect. Figure 5 is a benchmark calculation for the case of particles with size less than λ. Both the dipole limit (of the near field; see equations (16) and (17)) and the exact solution (Mie scattering; see equations (B.1) and (B.2)) are given. When the size is much smaller than the wavelength, as is the case for the 10 nm radius silver wire and protein vesicle shown in figure 5 (top), the dipole limit is almost coincident with the exact (Mie) solution. For the 50 nm radius silver wire in figure 5 (middle left), there is a small deviation between dipole limit and exact solutions, which is particularly apparent for the transverse component (E_x). For the 50 nm protein vesicle in figure 5 (middle right), the fields are more confined (with r^{-3} dependence) than in the case of the wire, and therefore differences between the approximate and the exact solutions are less apparent. For the 100 nm radius silver wire and protein vesicle shown in figure 5 (bottom), the dipole limit does not reproduce the exact solutions, even for the longitudinal component (E_z). In such cases, the use of the exact solution is desirable for accurate computation.

It is to be noted that the longitudinal components are more confined than the transverse components because at far distance they are mainly composed of the radial components of the

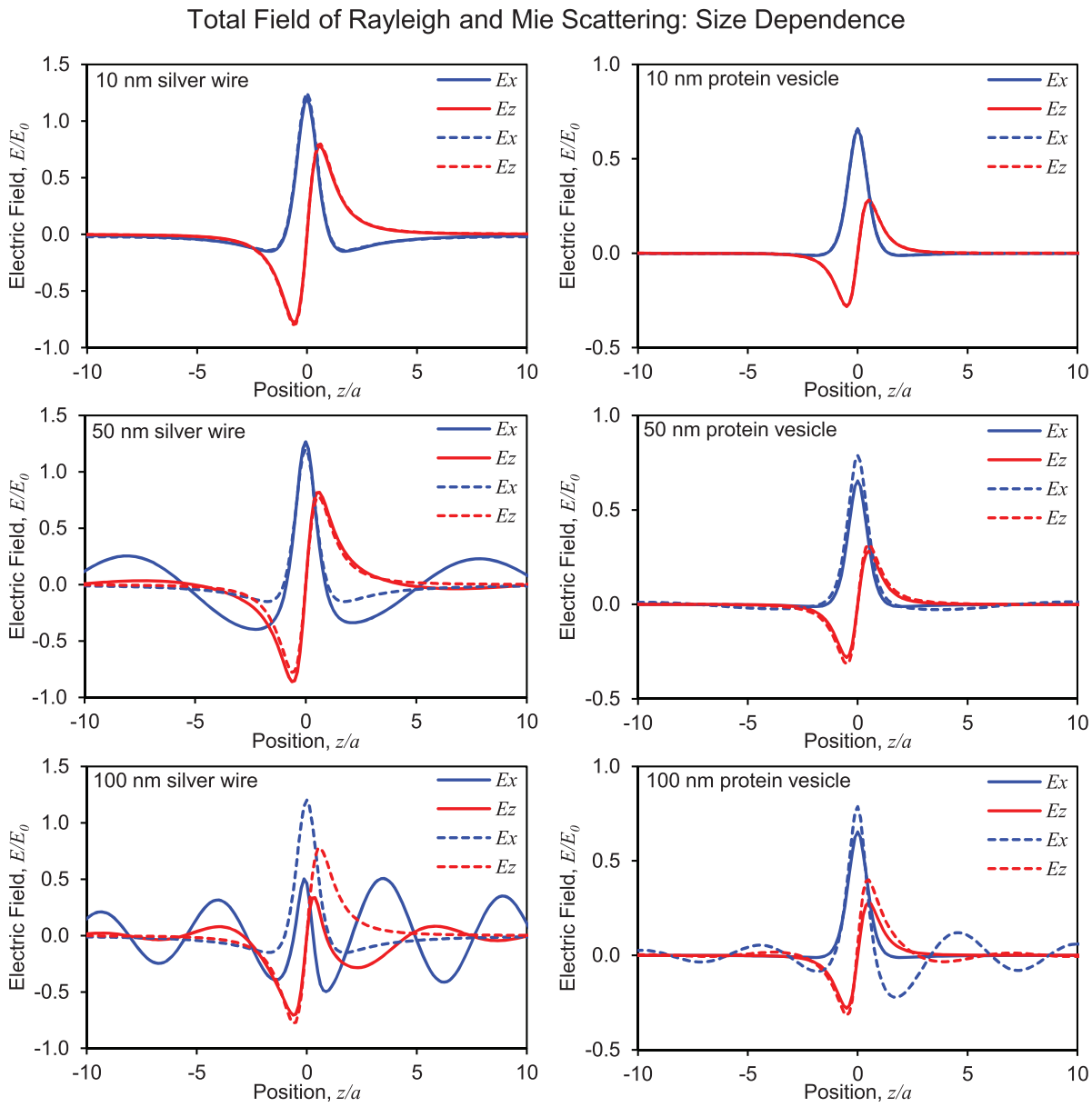

Figure 5. Rayleigh (dipole) and Mie (exact) total scattered fields. Comparison of the electric field components of the (Rayleigh) dipole approximation near-field limit with the (Mie) exact solution for silver nanowires (left) and spherical protein vesicles (right). The results were compared for radii of 10 nm (top), 50 nm (middle) and 100 nm (bottom).

scattered (spherical) wavelets, which decay faster than the angular components. The scattered wave results from reflection and refraction off the surface. Unlike evanescent modes on flat surfaces (metal plasmons and dielectric total internal reflection), which are confined due to dielectric constant mismatch, the scattered waves are geometrically confined around nanoscale materials. Consequently, the decay length of the field strength is determined only by the particle size for small spheres and cylinders and independent of the material (see section 4).

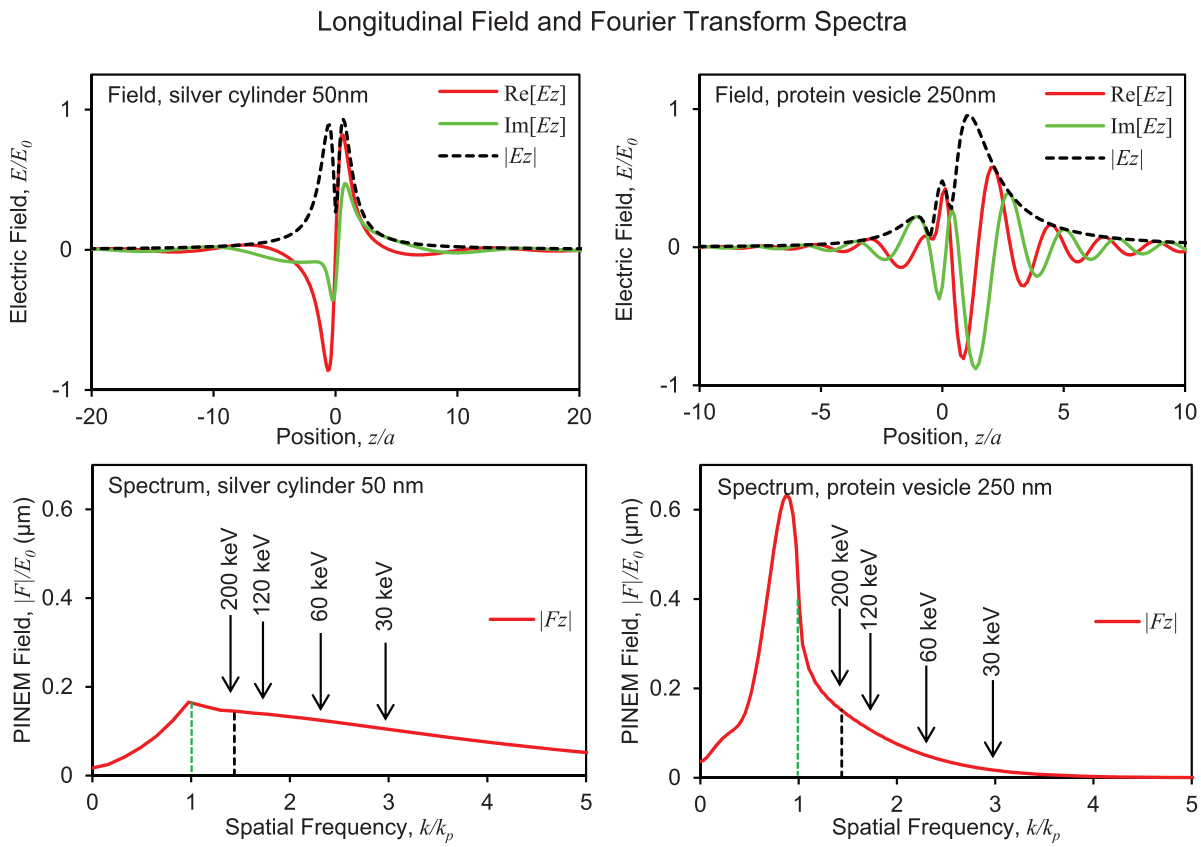

Figure 6. Longitudinal fields and their spatial frequency spectra. Normalized longitudinal components of the scattered electric field (top) and the field spectra (bottom) along the electron trajectory for (left) a 50 nm metal cylinder ($\tilde{n} = 0.05 + 3.31\mathrm{i}$) and (right) a 250 nm dielectric sphere ($\tilde{n} = 1.57$), at 519 nm illumination. Dotted lines represent the amplitude of the electric field, and solid lines represent the real and imaginary parts of the field. The positions of arrows indicate the spatial frequency changes required for electrons with energies of 200, 120, 60 and 30 keV to absorb a photon with 519 nm wavelength.

In figure 6, the theoretical calculations are presented for two cases studied experimentally by PINEM: the silver nanowire and the protein vesicle. The top panels show the amplitudes as well as the real and the imaginary parts of the longitudinal component, E_z, along the electron trajectory, at an impact parameter equal to the radius of the nanostructure. In the case of the metallic ($\tilde{n} = 0.05 + 3.31\mathrm{i}$) cylinder of 50 nm radius (left), the scattered electric field components are quite symmetric with respect to the z-coordinate. However, in the case of the dielectric ($\tilde{n} = 1.57$) sphere of 250 nm radius (right), the electric field is asymmetric with respect to the z-coordinate due to forward scattering enhancement (toward positive z), which is manifest in the Mie solution for particles of size comparable to or larger than the wavelength of the light. The light scattered from both metallic and dielectric nanostructures possess near-field components comparable in strength to that of the incident wave and extend over the length scale of the particle.

Since the magnitude of the PINEM field is proportional to the incident electric field, for plotting purposes we shall use the normalized PINEM field, $|\tilde{F}_z|/E_0$. Figure 6 (bottom) depicts the normalized Fourier transformed spectra, $|\tilde{F}_z(k)|/E_0$, of the scattered electric field shown in the top panels. The spectra are broad distributions because the electric fields are narrowly confined. This is analogous to the position-momentum uncertainty tradeoff (see figure 1 (top)) [17]. The E_z distribution near the small cylinder resembles a Lorentzian function such that its Fourier transform is an exponential-like function, whereas the E_z distribution near the small sphere resembles a Gaussian such that its Fourier transform is also a Gaussian-like function. Note that the difference in the field spectra between the 250 nm dielectric sphere and the 50 nm metallic cylinder is due to particle size rather than material composition or shape. For 519 nm illumination, the scattered field adjacent to the 250 nm particle exhibits a few optical cycles, whereas the field near the 50 nm particle has less than one cycle. In fact, the spectrum of a 50 nm dielectric cylinder (not shown) is similar to that of a metallic cylinder or sphere of the same radius.

The electric field spectrum $|\tilde{F}_z(k)|$ for the dielectric sphere of 250 nm radius displays a maximum around that of the free photon ($k = k_\mathrm{p}$) but is significantly broadened due to spatial confinement. At the spatial frequency that can couple with a 200 keV electron ($k = \Delta k_\mathrm{e} = 1.438 k_\mathrm{p}$), the magnitude in the distribution is less than the maximum but is still significant. It is this broadening that allows the momentum component required for electron–photon coupling (see figure 1 (top)). For a slower electron (smaller v_e and therefore larger $\Delta k_\mathrm{e} = \omega_\mathrm{p}/v_\mathrm{e}$), the Fourier transform component at $k = \Delta k_\mathrm{e}$ decreases for both spherical and cylindrical geometries (see figure 6 (bottom)). In the case of the sphere, $|\tilde{F}_z(k)|$ falls off quickly such that it becomes insignificant for incident electrons below 30 keV, while $|\tilde{F}_z(k)|$ decreases more slowly for the cylinder, although this difference arises from the difference in sphere and cylinder radius rather than the type of geometry. Henceforth, in order to compare with the experimental conditions, we define $F_z \equiv |\tilde{F}_z(1.438 k_\mathrm{p})|$, which is the magnitude of the PINEM field that can couple with our 200 keV electrons.

The electric field experienced by the propagating electron is due to the superposition of many spherical wavelets scattering from the nanostructure. It is to be recalled that the phase-matching condition is for what the electron experiences along its trajectory, not what the scattered photon actually possesses. When the field that the electron experiences is Fourier transformed, the amplitude of the spatial frequency component with the appropriate phase velocity to couple with the electron may be nonzero even if there are no photons propagating in free space with that spatial frequency. This is illustrated in figure 7. The incident wave enters the material, inside which the wavelength is shortened to $\lambda/\tilde{n}$. The induced polarization radiates spherical wavelets with alternating phase along θ, resulting in an angular modulation. Since the electric field of the spherical wavelet is transverse to its propagation ($\hat{r}$), it can coincide with the electron propagation direction ($\hat{z}$). Therefore, the electron effectively sees an alternating longitudinal electric field, which efficiently couples with its momentum, p_z. Note that if the particle size (dotted circle) becomes smaller than λ_p of the incident radiation shown, then the field polarization is consistent with the dipole (Rayleigh) approximation (figure 4).

In what follows, we shall investigate the behavior of F_z, the PINEM field and its spatial and temporal profiles, so we may examine the various dimensions of PINEM experiments: pulse duration, polarization, particle size, material and wavelength, as well as the degree of penetration (impact parameter). Since $F_z = F_z(\phi = 0)\cos\phi$, the dependence of PINEM on the

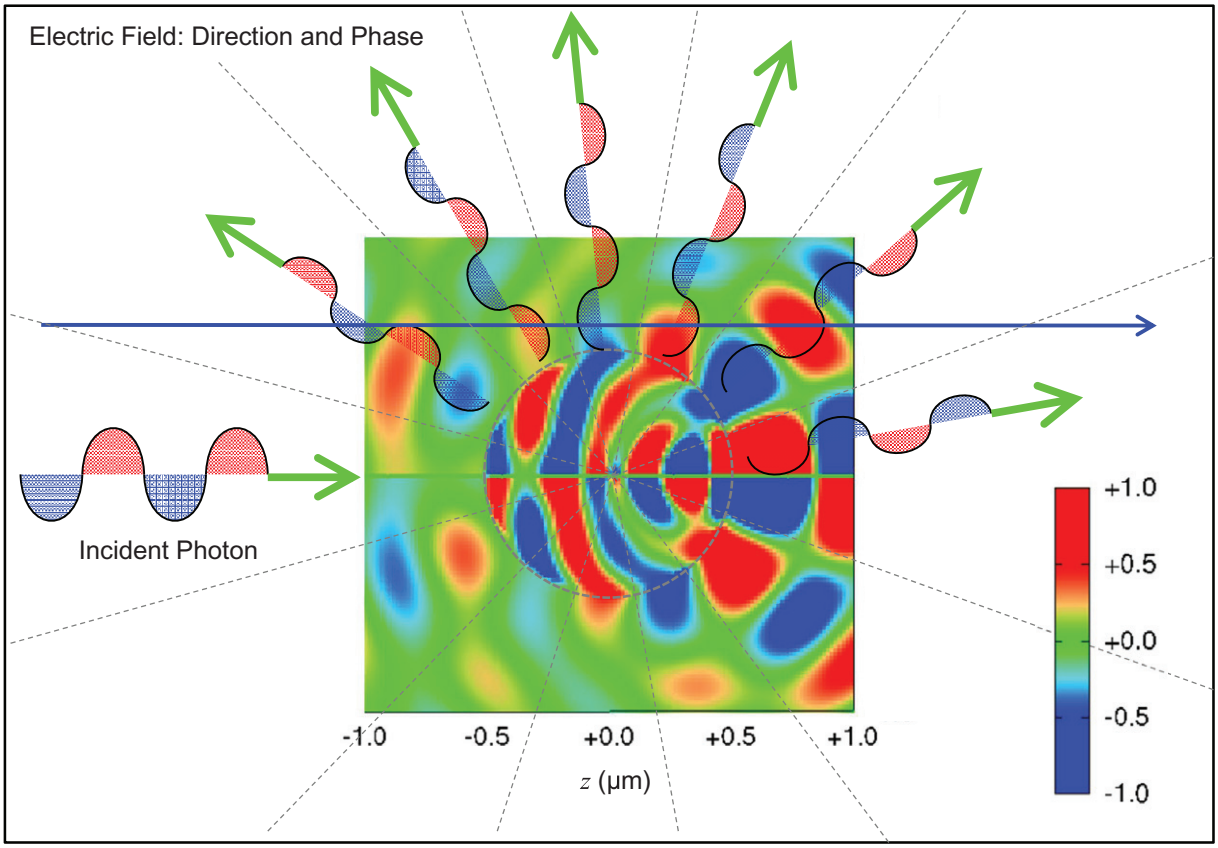

Figure 7. Field distributions and phases. Contour plot of the angular component, E_θ, of the light scattered from a dielectric ($\tilde{n} = 1.57$) sphere of 500 nm radius due to incident 519 nm radiation. The radial propagation of angularly modulated spherical wavelets is depicted as arrowed waves. Note that, for this particle size, there exists strong polarization within the particle.

polarization and laser fluence is apparent from theory and will be compared to experimental findings in section 5.

4.3.1. Temporal profile: pulse duration. The temporal profile of the PINEM intensity is expressed in equation (22) (see appendix A for details), with the duration of the pulses given by σ_e and σ_p (in g and ξ_n). In order to elucidate the importance of the temporal dependence on the order of absorption/emission by a net number of photons (n), which can be filtered in the energy domain, we consider here the weak interaction regime ($\Omega = eF_z/\hbar\omega \ll 1$ where $J_n(\Omega) \approx (1/n\,!)(\Omega/2)^n$). For this case, it follows that

$$P_n(z') \propto I^n \propto \exp\left[-\frac{n\,(z' + v_e\tau)^2}{2v_e^2\sigma_p^2}\right]. \tag{26}$$

This implies that the nth-order peak will have an effective duration of $\sigma_p/\sqrt{n}$ (assuming that $\sigma_p \ll \sigma_e$). In the strong interaction regime ($\Omega \gg n^2$), however, Bessel functions

become oscillatory,

$$J_n(\Omega) \approx \sqrt{\frac{2}{\pi\Omega}}\cos\left(\Omega - \frac{n\pi}{2} - \frac{\pi}{4}\right),$$

and the electron population distribution is reminiscent of a 'diffraction-type' pattern.

4.3.2. Spatial profile: polarization and the impact parameter. As mentioned above, the electric field of the scattered wave is proportional to $\cos\phi$ (see equations (B.1) and (B.2) for the exact solutions and equations (16) and (17) for the Rayleigh dipole near-field limit). Consequently, the PINEM field, F_z, also becomes proportional to $\cos\phi$, resulting in $\cos^2\phi$ polarization anisotropy in PINEM imaging.

Because the amplitude of the near field decreases away from the nanoparticle (the field decay lengths are $a/3$ and $a/2$ for small spheres and cylinders, respectively (see equations (16) and (17)), it is expected that the PINEM field F_z also decreases. Thus, electron–photon coupling becomes sensitive to the impact parameter of the electron trajectory, as is readily seen in the small-particle approximation.

For a small sphere (equation (24*a*)), K_1 is a reciprocal exponential-like function [29, 30], whereas for a small cylinder (equation (24*b*)), the PINEM field decays exponentially with increasing b. In figure 8 (top), the exact (normalized with respect to the incident wave electric field) PINEM field, F_z/E_0, is plotted as a function of the impact parameter, b, at $\phi = 0$ for 250 nm spheres and 50 nm cylinders of dielectric ($\tilde{n} = 1.57$) and metallic ($\tilde{n} = 0.05 + 3.31\mathrm{i}$) composition. For the electron trajectory going through the material interior ($b < a$), the PINEM field monotonically decreases as b goes to zero. When the trajectory is outside the material ($b > a$), the field decreases exponentially with b; typically, $1/e$ decay lengths of 68 and 80 nm for the 250 nm sphere and 50 nm cylinder, respectively, were obtained. Here, we emphasize that the decay length (not the magnitude) of F_z is independent of the material. The exponential decay behavior of F_z allows us to write

$$F_z(b, \varphi) \approx F_z(a, 0)\exp\left[-\frac{b-a}{\delta(a)}\right]\cos\varphi,$$

where δ is the decay length of the PINEM field.

In equation (24*a*), for a small sphere, F_z has a decay length of a, which is evaluated by logarithm-differentiation of equation (24*a*) as $\delta = -\lim_{b\to a}(\partial \log F_z/\partial b)^{-1} = a$. In equation (24*b*), for a small cylinder, the decay length is $\delta = (1/\Delta k_\mathrm{e}) = (\lambda_\mathrm{p}/2\pi)(v_\mathrm{e}/c)$ to the first order (see section 4 for the validity of equation (24*b*)). Figure 8 (middle) depicts the decay length of the PINEM field, δ, as a function of the particle radius, a, for the dielectric ($\tilde{n} = 1.57$) and metallic ($\tilde{n} = 0.05 + 3.31\mathrm{i}$) sphere and cylinder. We see that δ is identical for metal and dielectric materials, and determined only by the geometry, radius and light wavelength. Furthermore, the decay length for cylindrical nanostructures is mostly independent of the size, and is sensitive only to the wavelength of the incident light. In contrast, δ for spherical particles is indeed $\sim a$ for small a, and converges to an asymptotic value of $\sim$80 nm, which also coincides with that for cylinders.

The asymptotic decay length of 80 nm is somewhat larger than the theoretical estimation from the thin wire approximation, for which $(\lambda_\mathrm{p}/2\pi)(v_\mathrm{e}/c) = 58$ nm. In fact, it is found empirically that the asymptotic value is $\delta = (1/k) = (\lambda_\mathrm{p}/2\pi)$ for thick cylinders; the origin of this disparity will be investigated later. In figure 8 (bottom), the decay lengths of the PINEM

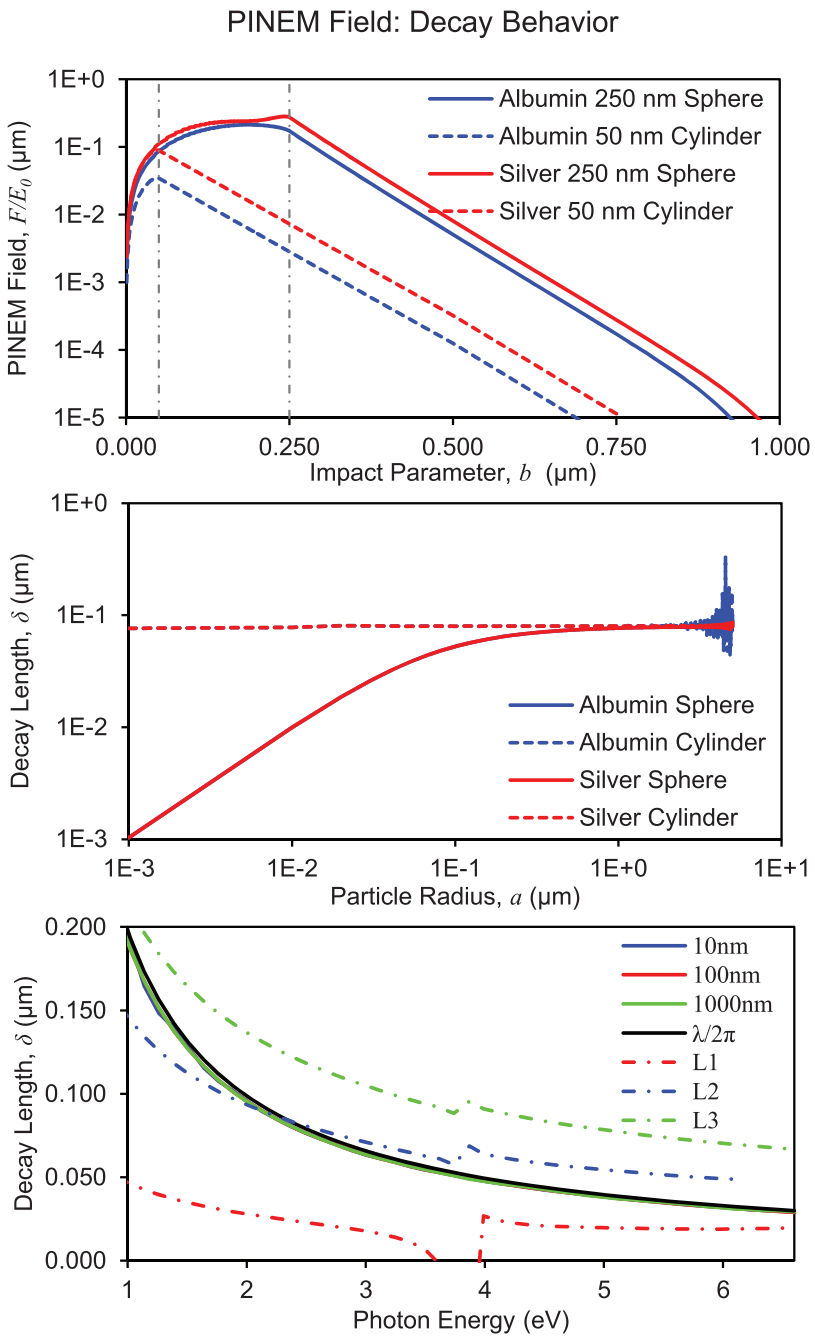

Figure 8. PINEM field decay behavior. (Top) The normalized PINEM field F_z/E_0 as a function of impact parameter, b, due to scattering of 519 nm incident light from 250 nm spheres (solid lines) and 50 nm cylinders (dotted lines) of dielectric ($\tilde{n} = 1.57$; blue) and metallic ($\tilde{n} = 0.05 + 3.31i$; red) composition. (Middle) The PINEM field decay length, δ, as a function of the particle radius, a, for spheres and cylinders of dielectric and metallic materials. (Bottom) The PINEM field decay length as a function of the photon energy for silver wires of various radii. The expected plasmonic-type behavior (equation (13)) is given for three modes L_1, L_2 and L_3. The value for $\lambda/2\pi$ (section 4.3.2) is shown for comparison.

field for silver cylinders of various thicknesses are plotted as a function of photon energy. Also plotted is $\lambda_p/2\pi$, which coincides with δ(a). The wavelength dependence of the decay length for silver wires clearly shows that $\delta = (1/k) = (\lambda_p/2\pi)$ at any size and wavelength. It is interesting to note that for the spherical geometry, the amplitude of the scattered electric field has a scattering depth of $\sim a/3$ in the small-particle limit (see equation (16)), but the PINEM field, F_z, has a decay length of $\sim a$. For the cylindrical geometry, on the other hand, even though the field strength decays over $\sim a/2$ for thin cylinders, F_z decays over $\lambda_p/2\pi$, independent of the cylinder radius.

4.3.3. Size dependence. The F_z/E_0 as a function of radius a, due to scattering of incident 519 nm light from spheres and cylinders of metallic ($\tilde{n} = 0.05 + 3.31\mathrm{i}$) and dielectric ($\tilde{n} = 1.57$) materials, at an impact parameter equal to the radius, is shown in figure 9 (top). For comparison, the Mie exact solution and the dipole near-field limit are shown for both geometries. For spheres, as expected, the dipole limit agrees with the exact solution for small particles, and begins to fail when the particle radius approaches the length scale of the incident light (near 100 nm). In the small radius regime, $F_z \propto a^3/b \approx a^2$, as predicted by equation (25*a*). F_z decays for spheres with radii bigger than 300 nm and, as the particle size becomes larger than the wavelength, the interferometric resonance effect [41] of different spherical modes leads to oscillatory behavior, which is particularly apparent for the dielectric material (see figure 9 (middle)).

The asymptotic behavior of F_z may be understood as follows. As seen in figure 6, the maximum amplitude of the scattered electric near field is always comparable to that of the incident light, regardless of the particle size, whereas the spatial extent of the field is comparable to the size of the particle. Although the spatial extent of the field increases as the particle size increases, the PINEM field, F_z, does not necessarily proportionally increase because the increased radius also affects the size of the confinement, which consequently affects the spectrum $\tilde{F}_z(k)$. As the particle size increases, the spatial frequency spectrum becomes narrower around $k = k_p$, therefore lowering the amplitude at $k = \Delta k_e = 1.438 k_p$. The oscillatory behavior is believed to arise from the interferometric resonance [41] of different spherical modes when the particle size becomes larger than the wavelength. Indeed, the same oscillatory feature is observed in the plot of the scattering efficiency (not shown). Therefore, the oscillations can be viewed as a geometric resonance of the electric field strength. For cylinders (equation (17)), the scattered electric field decays slowly (r^{-2}), and unlike the case for the spherical geometry, far-field components are not negligible in the PINEM field. However, the deviation is only 50 and 5% for cylinders with radii of 100 and 10 nm, respectively. In the dipole limit, $F_z \propto a^2$ as predicted by equation (25*b*).

Figure 9 (bottom) displays the geometry dependence of F_z as a function of the particle size for albumin ($\tilde{n} = 1.57$) and silver ($\tilde{n} = 0.05 + 3.31\mathrm{i}$) nanostructures. It is clear that F_z is much more sensitive to particle size than to material or geometry. Silver shows generally higher F_z values at any size and shape than the dielectric; this is due to the higher polarizability of metals (see section 4.3.4). For example, χ_s is 0.33 and $1.34 + 0.01\mathrm{i}$ for albumin and silver spheres, respectively. For bigger nanostructures, dielectrics display more pronounced structural resonances than metals, regardless of the shape, because light is refracted (penetrates) into the dielectric, while large metal particles mainly reflect the incident light. It is interesting to note that for both dielectric and metallic materials, resonance enhancement occurs at slightly different radii for cylinders as compared to spheres (see figure 9 (bottom)).

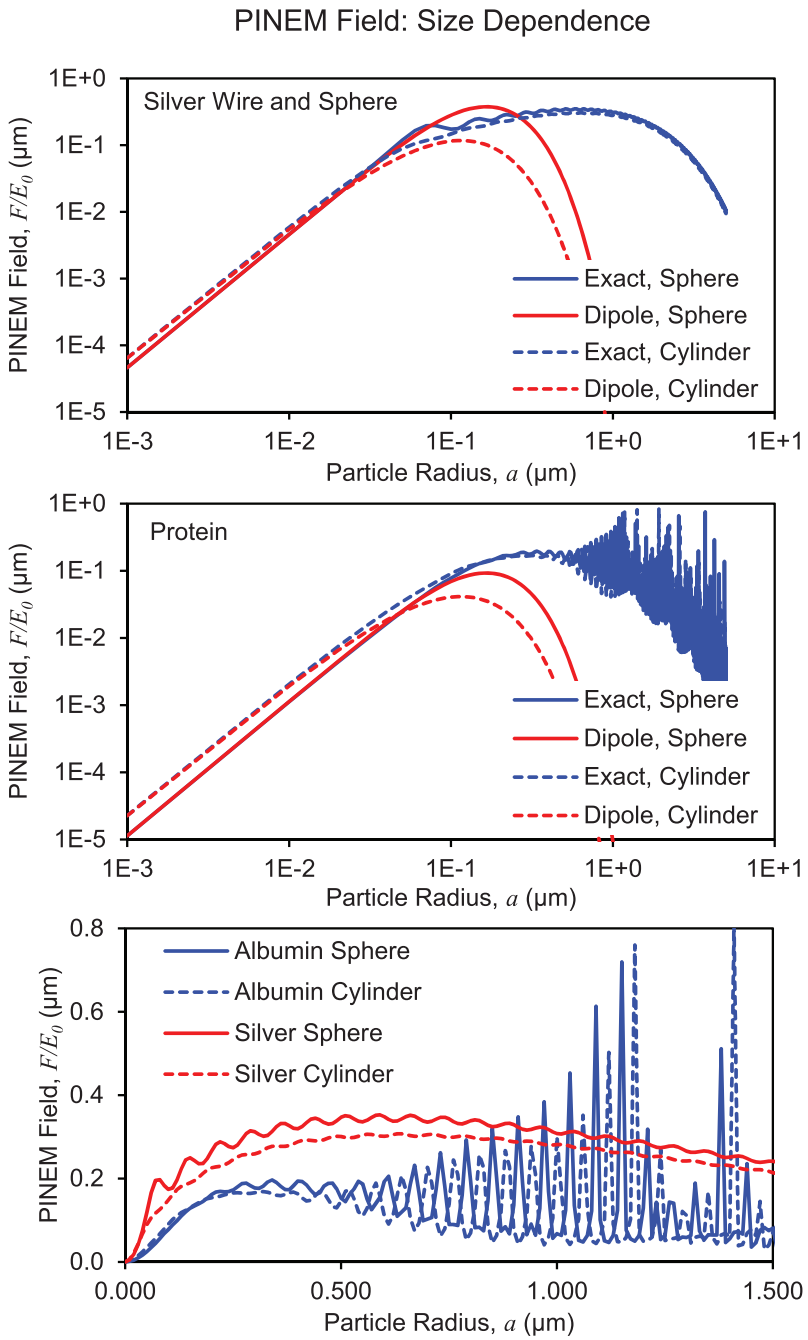

Figure 9. PINEM field size dependence. Log plots of F_z/E_0 for (top) metallic ($\tilde{n} = 0.05 + 3.31\mathrm{i}$) and (middle) dielectric ($\tilde{n} = 1.57$) nanostructures as computed from the (Mie) exact solution and the (Rayleigh) dipole, near-field limit as a function of the radius. The solid curves are for a sphere and the dotted ones are for a cylindrer-shaped structure; blue is for an exact solution whereas red is for the dipole limit. (Bottom) The linear plot of the PINEM field as a function of radius for the different materials and geometries are shown using the exact solutions. The solid curves are for a sphere and the dotted ones are for a cylinder-shaped structure; blue is for dielectric whereas the red is for metallic material.

4.3.4. Dielectric versus metallic materialst. We have compared the scattering of dielectric and metallic nanomaterials in figures 6–9 in previous subsections. Here, by 'a dielectric' we mean a material that has a positive real refractive index (positive dielectric function), and a metal as a material that has an imaginary refractive index (negative dielectric function). Both materials produce similar responses, although the amplitude is larger for metals due to higher polarizability. This is most easily seen in the small radius limit, where the scattered electric field, and therefore F_z, is proportional to the polarizability α. The enhancement of the polarizability in metals can be understood once α is expressed as a function of $\varepsilon(\omega)$, the dielectric constant: $\alpha = 4\pi\varepsilon_0\chi_s a^3$ with $\chi_s = (\varepsilon(\omega)-1)(\varepsilon(\omega)+2)^{-1}$ for spheres, and $\alpha = 4\pi\varepsilon_0\chi_c a^2$ with $\chi_c = (\varepsilon(\omega)-1)(\varepsilon(\omega)+1)^{-1}$ for cylinders. From these expressions, we can see that metallic materials can enhance α (and therefore F_z) due to their negative dielectric constants; the resonant enhancement is achieved for values of the incident ω such that $\varepsilon(\omega)$ approaches -2 in the spherical geometry (known as the Fröhlich resonance [25]) or -1 in the thin cylindrical geometry. For larger particles, the expression for polarizability is not straightforward due to interference effects.

Figure 10 (left) shows the calculated F_z/E_0 as a function of refractive index $\tilde{n} = \sqrt{\varepsilon}$, near dielectric nanostructures (sphere and cylinder) of large (top) and small (bottom) sizes. For $\tilde{n}$ close to 1, the light scattering is proportional to $\tilde{n}^2 - 1$, and the electron–photon coupling vanishes at $\tilde{n} = 1$. For significantly larger $\tilde{n}$, the calculated plot of F_z/E_0 shows sharp features due to structural resonances of different spherical and cylindrical modes [41]. The position of the resonance feature is slightly different for spheres and cylinders due to geometry-specific resonance conditions; the same effect was observed in figure 9. Since the structural resonance occurs in the same way as interference inside an interferometer, it is expected to depend on the the size of the nanostructure, the refractive index and the wavelength of light.

4.3.5. Wavelength dependence. For dielectric materials that are excited off-resonance, or with weak on-resonance absorption, $\tilde{n}$ is weakly dependent on the incident light frequency, whereas for metals, $\tilde{n}$ is inversely proportional to the incident light frequency in the visible range ($\tilde{n} \propto i/\omega$; see the discussion of the Drude model in section 2). Figure 10 (right) depicts the calculated F_z/E_0 as a function of photon energy, near dielectric (top) and metallic (bottom) nanostructures of different shapes and sizes. Here, the refractive indices of the dielectric and metallic materials were interpolated from the experimental data for bovine serum albumin [42], graphite [43], silver and gold [27]. In figure 10 (left), F_z changes slowly and monotonically in the region near $\tilde{n} = 1.57$ for dielectric spheres and cylinders. Consequently, no resonance effect is seen for incident light frequencies corresponding to this range of $\tilde{n}$. On the other hand, a sphere with a larger radius or refractive index can show strong wavelength dependence due to the interferometric or structural resonance [41] (not shown here). However, graphite, which has a large refractive index, $2.53 + 1.16i$ at 519 nm, does not show this resonance effect because of the large imaginary part of $\tilde{n}$ (see figure 10 (top right)). In figure 10 (bottom right), 50 nm metallic cylinders show an enhancement at $\sim$3.5 eV for silver and $\sim$2.5 eV for gold, which corresponds to the cylindrical resonance at $\tilde{n}^2 = -1$ in the small cylinder limit (see equations (24*b*) and (17)), whereas large cylinders do not exhibit this strong Fröhlich-type resonance.

Figure 11 depicts the calculated spectroscopic (absorption and scattering) efficiencies as a function of incident photon energy for various sizes and geometries of albumin, graphite, silver and gold nanostructures. It is to be noted that the scattering efficiency includes all the contributions for outgoing wavelets, such as refraction and reflection, while the absorption

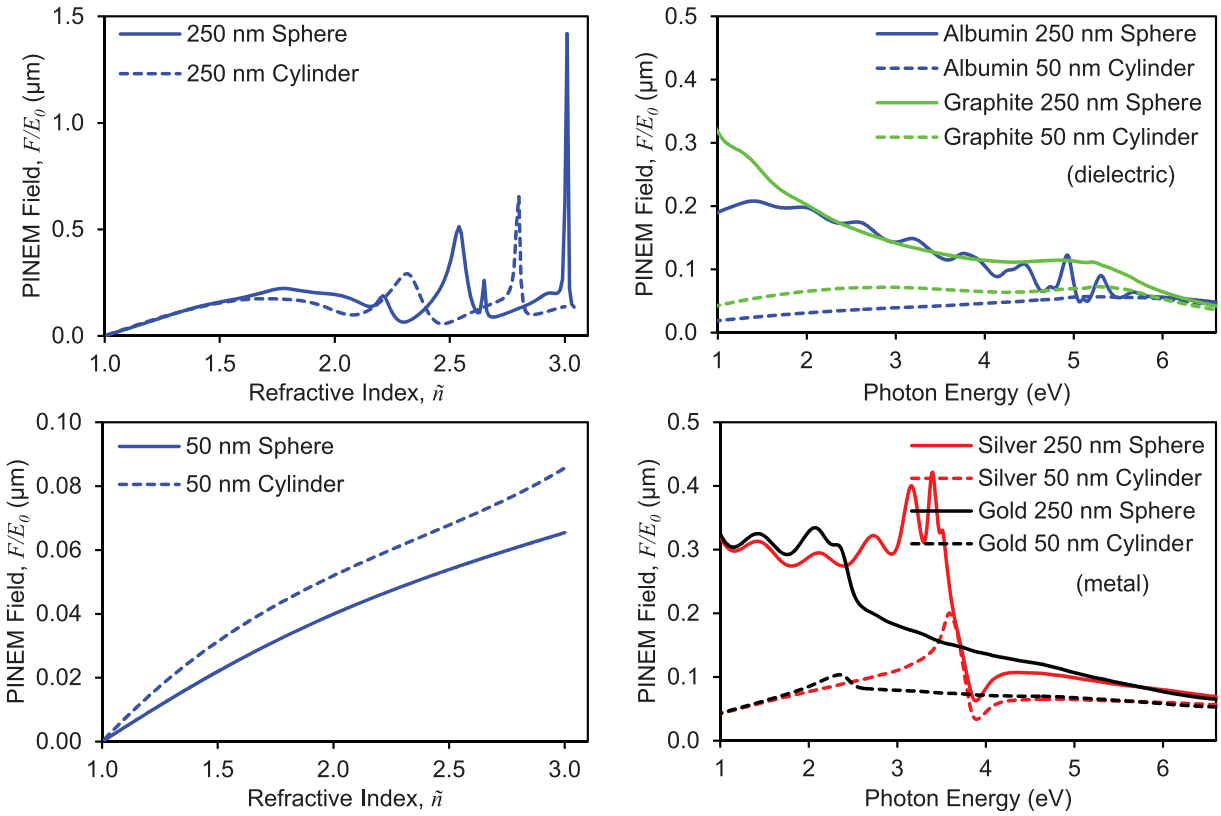

Figure 10. Dependence of the PINEM field on the material and the photon excitation. (Left) The normalized PINEM field F_z/E_0 due to scattering of 519 nm light from dielectric spheres (solid line) and cylinders (dotted lines) of (top) large and (bottom) small radii, plotted as a function of refractive index. (Right) The normalized PINEM field F_z/E_0 for (top) dielectric and (bottom) metallic spheres and cylinders of 250 and 50 nm radii, as a function of incident photon energy. The refractive indices of bovine serum albumin, graphite, silver and gold were interpolated from the experimental data in the literature (bovine serum albumin [42], graphite [43], silver and gold [27]).

efficiency is determined by the interior electric field and extinction coefficient. It is readily seen that the PINEM fields in figure 10 are directly correlated with the scattering efficiencies shown in figure 11, which is intriguing because F_z is calculated along a path in the vicinity of the particle, whereas the scattering efficiency is the sum of all outgoing wave contributions averaged over the entire solid angle.

Albumin has a negligible extinction coefficient (imaginary part of refractive index), and absorption is insignificant for incident photon energy less than 6 eV, regardless of the particle size. Graphite shows little change in scattering and absorption in the photon energy range plotted, because its absorption energy is much higher. On the other hand, small metallic particles show dominant absorption, with an enhancement around the Fröhlich resonance at ∼3.5 eV for silver and ∼2.5 eV for gold in figure 11 (right). For small metallic nanostructures, light can

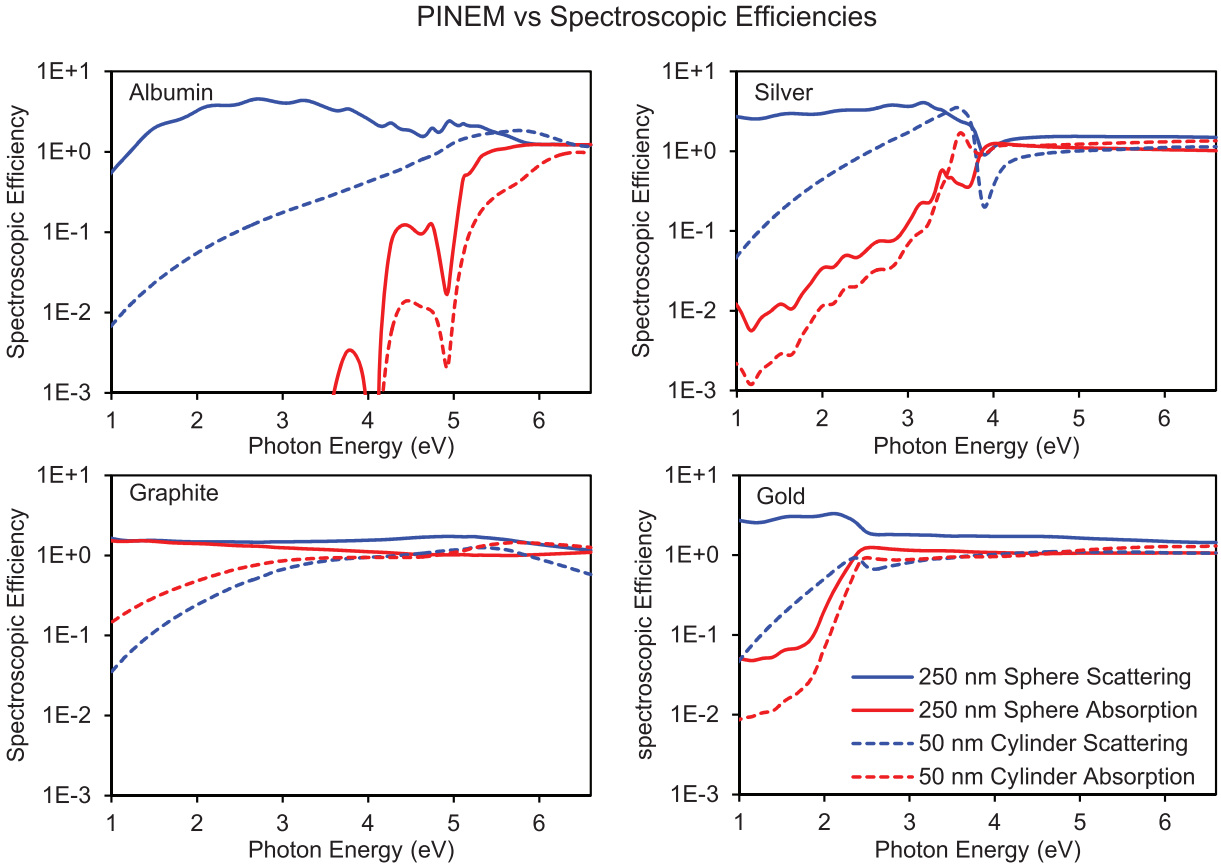

Figure 11. PINEM field versus spectroscopic efficiencies. Spectroscopic efficiencies of scattering (blue) and absorption (red) for 50 nm cylinders (dotted line) and 250 nm spheres (solid line) of albumin, graphite, silver and gold as a function of the incident photon energy.

effectively excite the entire material, regardless of photon energy. The figure shows that large metallic particles behave like a bulk metal and reflect light of frequency below that of the surface plasmon. Above the surface plasmon frequency, the bulk metal becomes transparent and the whole particle is excited by the incident light, resulting in scattering and absorption.

5. Comparison with experimental results

In this section, we compare the above theoretical results with the experimental findings, recently obtained with our second generation, ultrafast electron microscope (UEM-2) [1, 2] and others obtained by Barwick and Flannigan of this laboratory. Of special interest are the fields imaged by energy filtering and the temporal and polarization behavior. For a single impact parameter (b) and polarization angle (ϕ), equation (23) can be used to simulate the PINEM image as well as the electron energy gain spectum (EEGS) and electron energy loss spectrum (EELS). However, in the experiment, the EEGS/EELS is collected with all possible b and ϕ within the window aperture, w, whereas the PINEM image is acquired by summing all the energy-gained electrons at each fixed b and ϕ. In order to compare theory and experiment, those integrations need to be performed.

The PINEM image intensity summed over n is simply given by

$$I_{\mathrm{PINEM}}(b,\phi)=\sum_{n=+1}^{\infty}P_n(b,\phi)=\frac{1}{2}\{1-P_0(b,\phi)\}, \tag{27}$$

with P_n of equation (22) integrated over b and ϕ at the temporal delay, τ, giving

$$P_{\mathrm{EEGS}}(n)=\frac{1}{\pi\left(w^2-a^2\right)}\int_0^{2\pi}\mathrm{d}\phi\int_a^w\mathrm{d}b\,b\int_{-\infty}^{+\infty}\mathrm{d}z'$$
$$\times\left|g(z',-\infty)J_n\left(\frac{-e}{\hbar\omega_{\mathrm{p}}}|\tilde{F}_z(b,\phi)|\exp\left[-\frac{(z'+v_{\mathrm{e}}\tau)^2}{4v_{\mathrm{e}}^2\sigma_{\mathrm{p}}^2}\right]\right)\right|^2, \tag{28}$$

where w is the radius of the window. Here, the electron transmission inside the material is made negligible, which is valid for thick or dense structures, such that the integration is done from a to w; for imaging, the transmitted fraction is explicitly considered as shown below in sections 5.1 and 5.2. As seen in the previous section, the $\tilde{F}_z$ term can be approximated as $\tilde{F}_z(b,\phi)\approx\tilde{F}_z(a,0)\exp[-(b-a)/\delta]\cos\phi$ for spheres, where δ is the $1/e$ decay length. Although equation (28) needs to be numerically integrated, in equation (23), the $\tilde{F}_z$ terms in the summation can be analytically integrated, and the fraction can be expressed as an infinite sum (see appendix A for details),

$$P_{\mathrm{EEGS}}(n)=\sum_{j=0}^{\infty}\sum_{k=0}^{\infty}D_{jk}^{n}C_j^nC_k^{n^*}(1+S_{njk}R_\sigma^2)^{-1/2}\exp\left[-\frac{S_{njk}R_\tau^2}{2(1+S_{njk}R_\sigma^2)}\right]. \tag{29}$$

5.1. Spatial dependence

One of the main features of the PINEM effect is the spatial localization of electron–photon interactions near the nanoscale surface. Figure 12 (top) shows the PINEM image of a single carbon nanotube (147 nm diameter) at zero time delay ($\tau=0$) [1]. In figure 12 (bottom), the transverse cross-sectional profile of the PINEM image, which is averaged along the carbon nanotube axis, is displayed. Also plotted is the calculated PINEM profile, using equation (23), with the scattered electric field obtained using equation (B.2) for a cylinder, and summed over the energy-gained electron populations using equation (27). The profile exponentially decays from the sides of the wire (at $\sim$74 nm), as predicted by the impact parameter dependence. The dip at the center is the combined effect of transmission of electrons and the field of PINEM. We note here that the nanotube itself is the 'background' and the field is 'lighted up' in the image contrast.

5.2. Polarization

Another feature of PINEM is its dependence on the polarization of the electric field of the incident light. Figure 13 (top) shows the density plot of the PINEM image of a single protein vesicle [2], with the electric field of the incident wave indicated by the arrow. Figure 13 (bottom) displays the calculated PINEM image, where the population is obtained using equation (23),

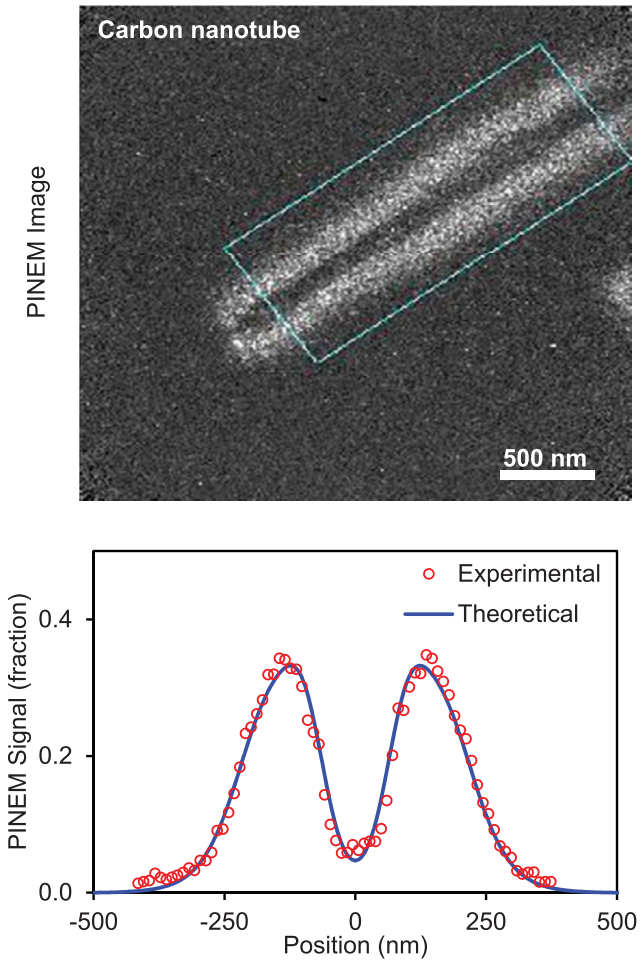

Figure 12. Experimental and theoretical PINEM spatial dependences. (Top) The experimental PINEM image of a single carbon nanotube (147 nm diameter). (Bottom) The experimental and theoretical transverse cross-sectional profiles of the PINEM image. Both the PINEM intensity and the fraction of the transmitted intensity, in this case taken to be 0.16, are shown.

with the scattered electric field, in this case, determined using equation (B.1) for a sphere and then summed over energy-gained electron populations using equation (27). The polarization dependence of $\cos^2\phi$ is in a good agreement with the experiment. Similar polarization effects were observed for other materials, including nanotubes and biological cells.

5.3. Energy spectrum

The energy gain/loss observed for nanostructures on the femtosecond time scale [1] can be reproduced theoretically. Figure 14 shows the theoretical and experimental EEGS and EELS for a single silver wire and a protein vesicle [2]. It is to be noted that figure 14 (top) is for a single silver wire, whereas the published EEGS/EELS data are for a cluster of silver wires

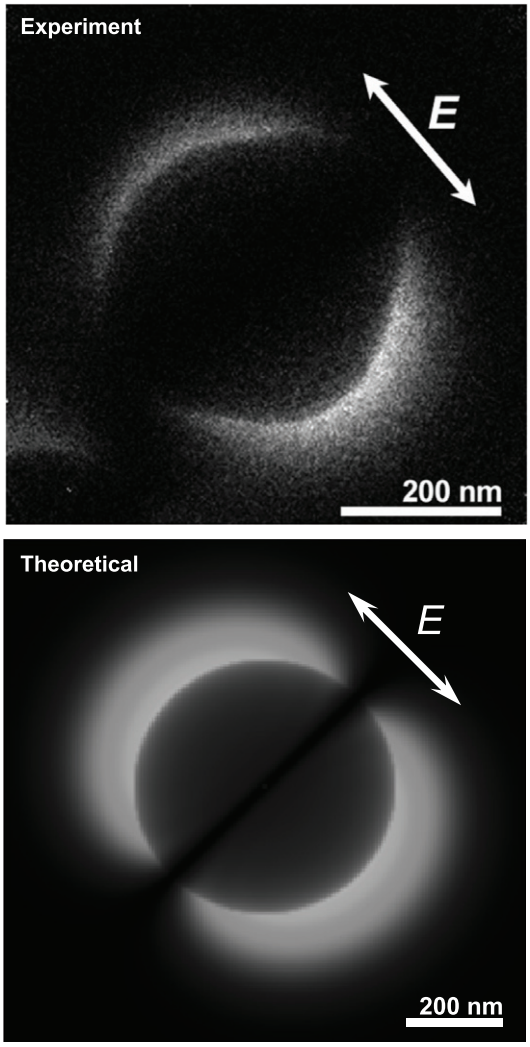

Figure 13. Experimental and theoretical PINEM polarization dependences. Density plots of (top) the experimental PINEM image of a single protein vesicle (∼150 nm radius) and (bottom) the theoretical PINEM image. We note that the theoretical image shows the $\cos^2\phi$ dependence and in the experimental image such dependence must be augmented with the topology of the vesicle, which is not exactly spherical [2].

unlike those obtained for the image [1]. The fraction of the nth order peak was calculated using equation (29) at $\tau = 0$, with the other parameters obtained by fitting the temporal dependence (see section 5.4). The widths and peak separations are obtained from fitting the experimental data with Voigt profiles. Theory and experiment show good agreement. The calculation is self-consistent in the sense that the fluence and pulse widths were obtained from the experimental results fitted in figure 15, and the same parameters were used to obtain the energy spectra.

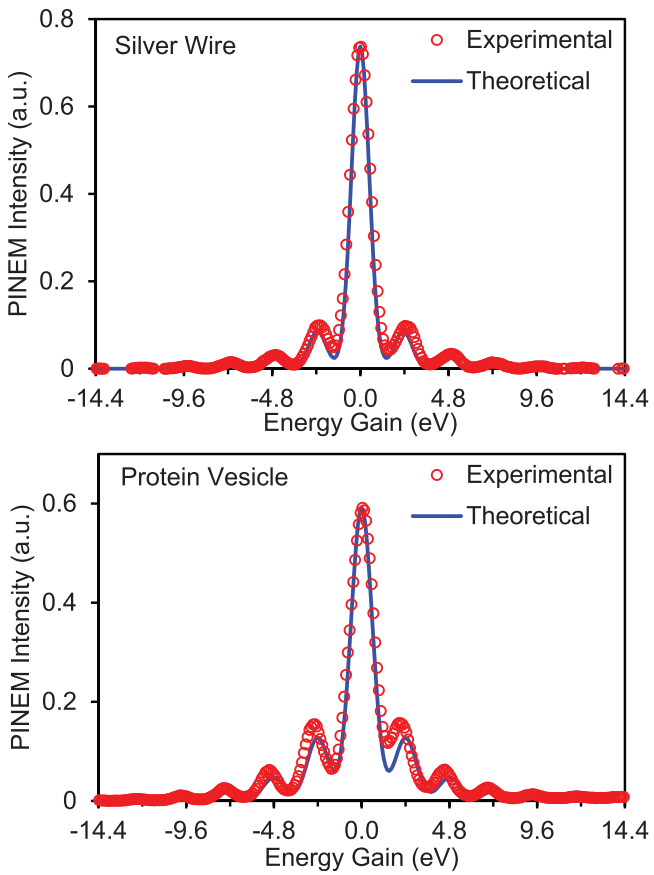

Figure 14. Experimental and theoretical EEGS/EELS spectra of PINEM. (Top) A single silver wire and (bottom) a single protein vesicle. (See text.)

5.4. Temporal delay and pulse duration

One of the intriguing aspects of PINEM was the dependence of the nth-order energy gain on the temporal delay [1, 2]. Equation (23) shows that, for fixed b and ϕ, different order peaks are indeed dependent on temporal delay and the peak order, with the amplitude being explicitly dependent on the parameters involved. Equation (29) shows that the total EEGS/EELS spectrum, which is averaged over b and ϕ, also displays the temporal delay dependence. In figure 15 (top), the experimental time dependence of the EEGS/EELS for a single protein vesicle [2] is compared to the theoretical results, $\Omega = eF_z/\hbar\omega_p = 6.7$, $\sigma_p = 108$ fs, $\sigma_e = 238$ fs, and $w = 347$ nm; the peak power density is 4 GW cm^{-2} (see table 1); this fluence agrees with the characteristics of the focused beam within a factor of two. The Gaussian widths are 288, 265, 255 and 249 fs for the first-, second-, third- and fourth-order energy-gained electron peaks, respectively.

In figure 15 (middle), the time dependence of the EEGS of a single silver wire is compared to the experiment, giving $eF_z/\hbar\omega_p = 4.7$, $\sigma_p = 209$ fs, $\sigma_e = 267$ fs and $w = 399$ nm; the peak power density is 3 GW cm^{-2} (see table 1). The temporal widths, σ_τ, are 407, 341, 310 and 295 fs for the first four orders. In figure 15 (bottom), similarly, the time dependence of the EEGS of a

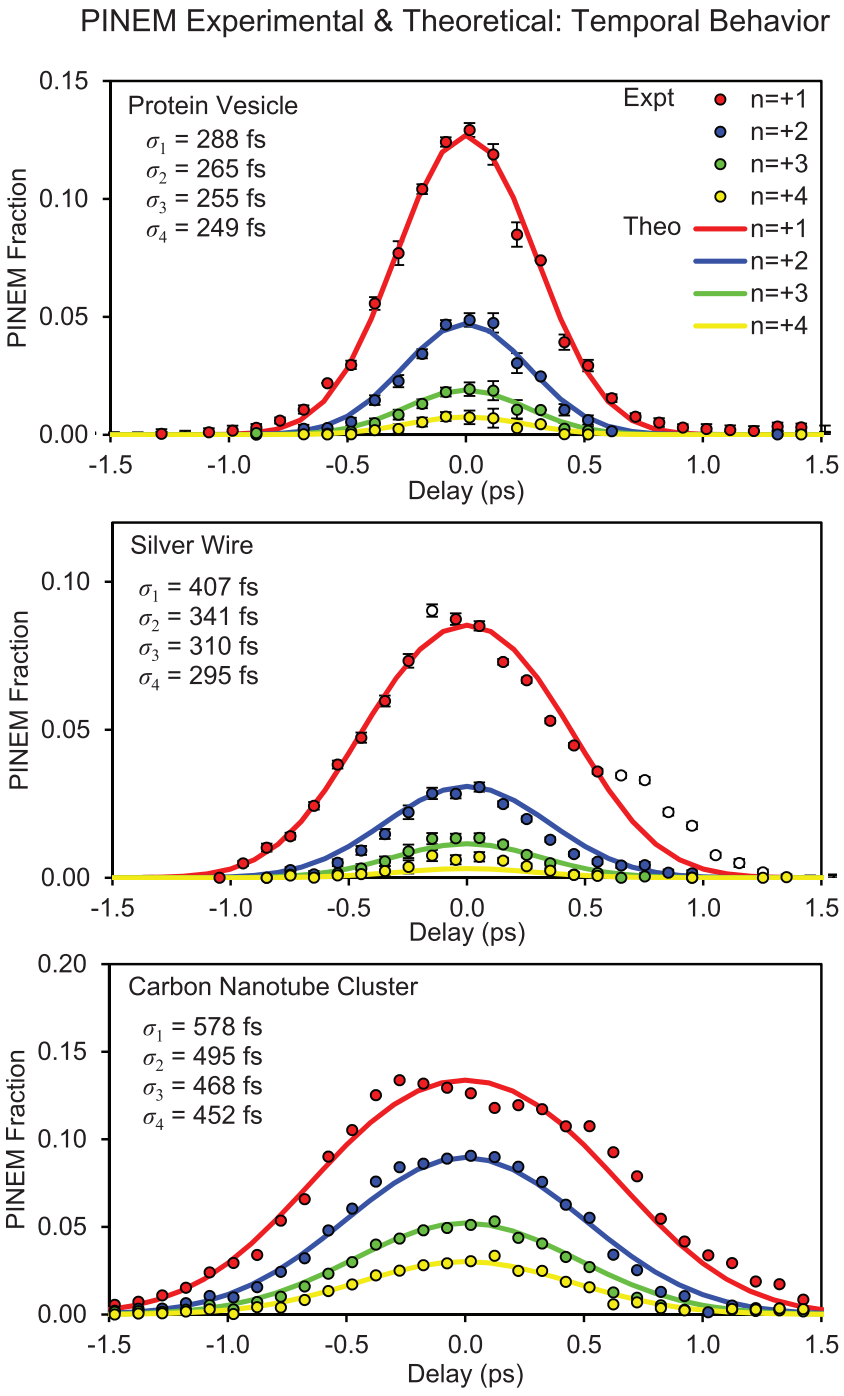

Figure 15. PINEM experimental and theoretical temporal behavior: the experimental (symbols) and theoretical (curves) fractions of electrons that absorb n net photons for (top) a protein vesicle, (middle) a single silver wire and (bottom) a cluster of carbon nanotubes, as a function of temporal delay, τ, between the electron packet and laser pulse. Note the narrowing in time as n increases.

Table 1. Theoretical parameters for EEGS/EELS calculations of the protein vesicle, silver wire and carbon nanotube.

	Protein vesicle	Silver wire	Carbon nanotube
$\Omega = eF_z/\hbar\omega$[a]	6.7 ± 0.6	4.7 ± 0.4	7.5 ± 1.2
σ_p (fs)	108 ± 4	209 ± 22	194 ± 4
σ_e (fs)	238 ± 4	267 ± 36	423 ± 18
w (nm)	347 ± 12	400 ± 34	165 ± 16
a (nm)	250	50	70
δ (nm)	68	80	80
F/E_0 (μm)	0.13	0.089	0.098
E_0 (V m^{-1})	1.2×10^8	1.1×10^8	1.8×10^8
U[b] (mJ cm^{-2})	1.1	1.9	4.4

[a] The errors reported here are two standard deviations (95% confidence level).
[b] U is the energy density of the pulse

carbon nanotube cluster is compared to the experiment [1], giving $eF_z/\hbar\omega_p = 7.5$, $\sigma_p = 194$ fs, $\sigma_e = 423$ fs and $w = 165$ nm; the peak power density is 9 GW cm^{-2} (see table 1). The temporal widths, σ_τ, are 578, 495, 468 and 452 fs for the first four orders. For imaging involving multiple tubes, the field is enhanced.

The apparent time dependence can be readily seen in equation (23). In the weak interaction limit, the probability can be approximated as the first term ($j = 0$ and $k = 0$) in the sum and the temporal behavior is a Gaussian function with effective width of $\sigma_\tau \approx \sqrt{\sigma_e^2 + (1/n)\sigma_p^2}$ for $n > 0$. For a strong interaction, the sequences in the summation (due to C_j^n and C_k^n terms) are alternately positive and negative, and therefore the effective width is somewhat wider than predicted for the weak interaction limit.

5.5. Fluence effect: kinetics, incoherent-coupling model

Figure 16 (top) depicts the experimental power dependence of the EEGS probabilities for a single silver nanowire, which shows the fractions of electrons that absorb up to six net photons. Figure 16 (middle) describes the (b-summed) theoretical fluence dependence of the EEGS probabilities for a single silver wire at $\tau = 0$ (10^{11} W cm^{-2} corresponds to $eF_z/\hbar\omega_p \sim 25$); note that the higher this value the larger the population in PINEM. Within the range plotted, the (intensity) oscillation characteristic of the Bessel function dependence is washed out because of b-summing, and the curves converge to an asymptotic value.

In equation (22), the probability of absorbing n net photons is proportional to the square of the Bessel function, J_n. The Bessel function is cosine-like, and therefore the population exhibits oscillatory behavior with respect to the fluence of photons. This oscillatory behavior is suppressed when the signal is summed over impact parameters (see figure 17). Figure 18 depicts the calculated EEGS/EELS of the silver wire at three different fluences and including b-summing. When the fluence reaches zero (figure 18 (top)), the EEGS/EELS contains only the zero-loss peak. For medium fluences (figure 18 (middle)), electrons that absorb/emit more than ten photons are observed. For relatively large fluences (figure 18 (bottom)), electrons with up

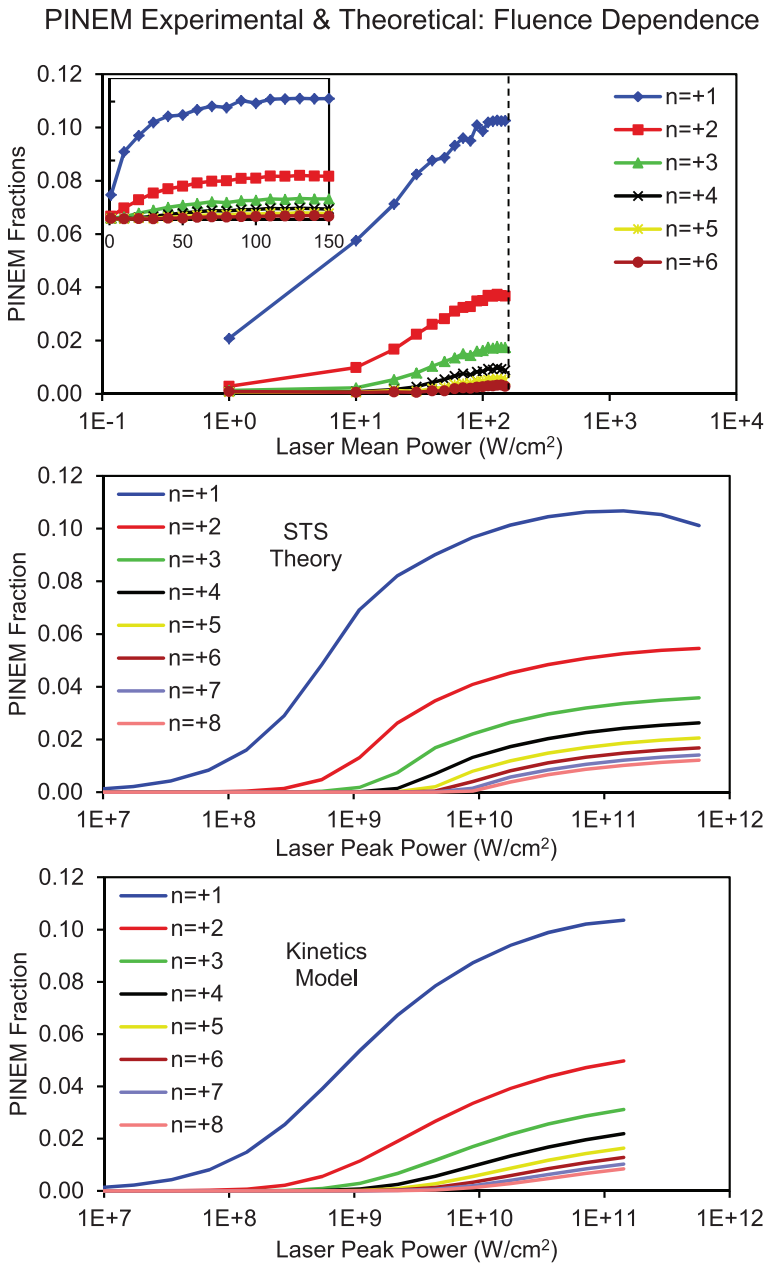

Figure 16. Dependence of PINEM on fluence. The temporally averaged and b-summed electron gain fraction at $\tau = 0$ for silver wire is shown. (Top) Experimental data (and in linear scale as an inset), as well as theoretical results calculated using (middle) STS (equation (29)) and (bottom) kinetic models (equation (C.13)). The summations of alternating sequences in equations (29) and (C.13) are slow to converge, and in practice the numerical summation may be unstable due to truncation errors. With 64-bit precision, which corresponds to about 16 significant digits, populations for $e\,|F_z|/\hbar\omega_p \sim 20$ (5.6×10^{10} W cm^{-2}) can be safely evaluated, and similarly with 80-bit precision, populations for $e\,|F_z|/\hbar\omega_p \sim 25$ (8.7×10^{10} W cm^{-2}) can be evaluated. For this reason, we used GNU bc software [53] for arbitrary precision arithmetic calculations, with precision set to 100.

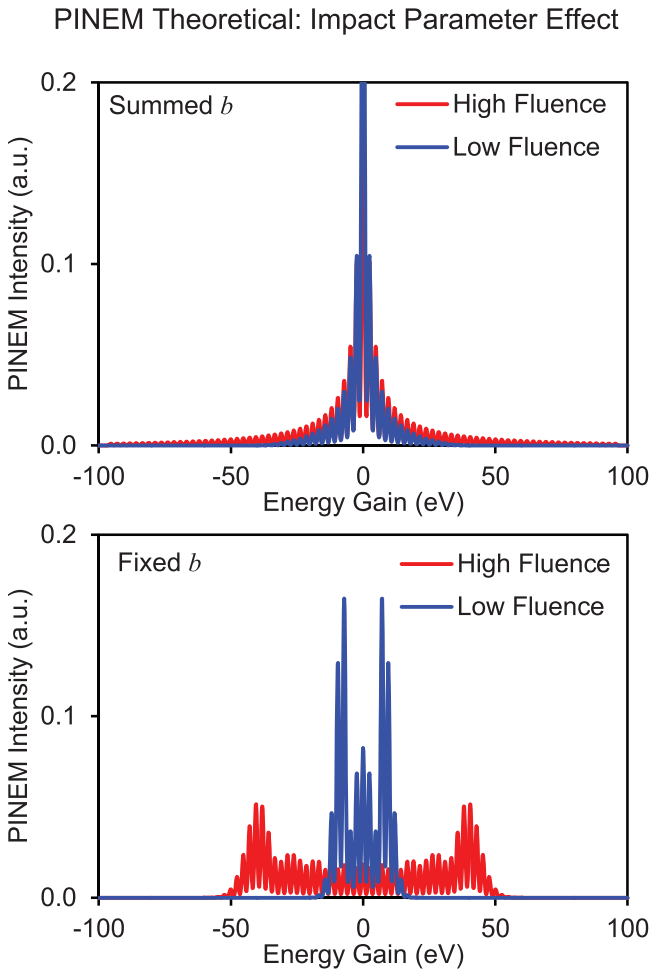

Figure 17. Dependence of PINEM on the fluence and impact parameter. Dependence of the EEGS/EELS spectrum on b-summing calculated for a single silver wire (50 nm radius). (Top) Summed over the impact parameter, b, at low (3.6×10^{10} W cm^{-2} peak power) and high (5.7×10^{11} W cm^{-2}) fluences and (bottom) for a fixed b at low (4.5×10^{9} W cm^{-2}) and high (1.5×10^{14} W cm^{-2}) fluences.

to 40 photons absorbed/emitted can be observed, although their amplitudes decrease, reaching less than 1% of the zero-loss peak. The theoretical results in figure 18 satisfactorily reproduce the experimental data presented in figure 19.

Although all of the above STS calculations dealt with coherent waves and their possible phases and interferences, it is interesting to compare the results with those obtained from kinetics, which describe an incoherent-coupling model solely given by the statistics of photon absorption/emission. In this case, the photon exchange is described as random collisions between the electron and scattered photons; the formulation of this model is given in appendix C. The model may be justified for an electron packet with a very short coherence length (less than the skin depth of the PINEM field ($\sim$100 nm)) or when using an incoherent light source. The incoherent-coupling model does not lead to the oscillatory behavior seen in the coherent-coupling theory (STS) discussed above (see figure 16 and appendix C for details). When

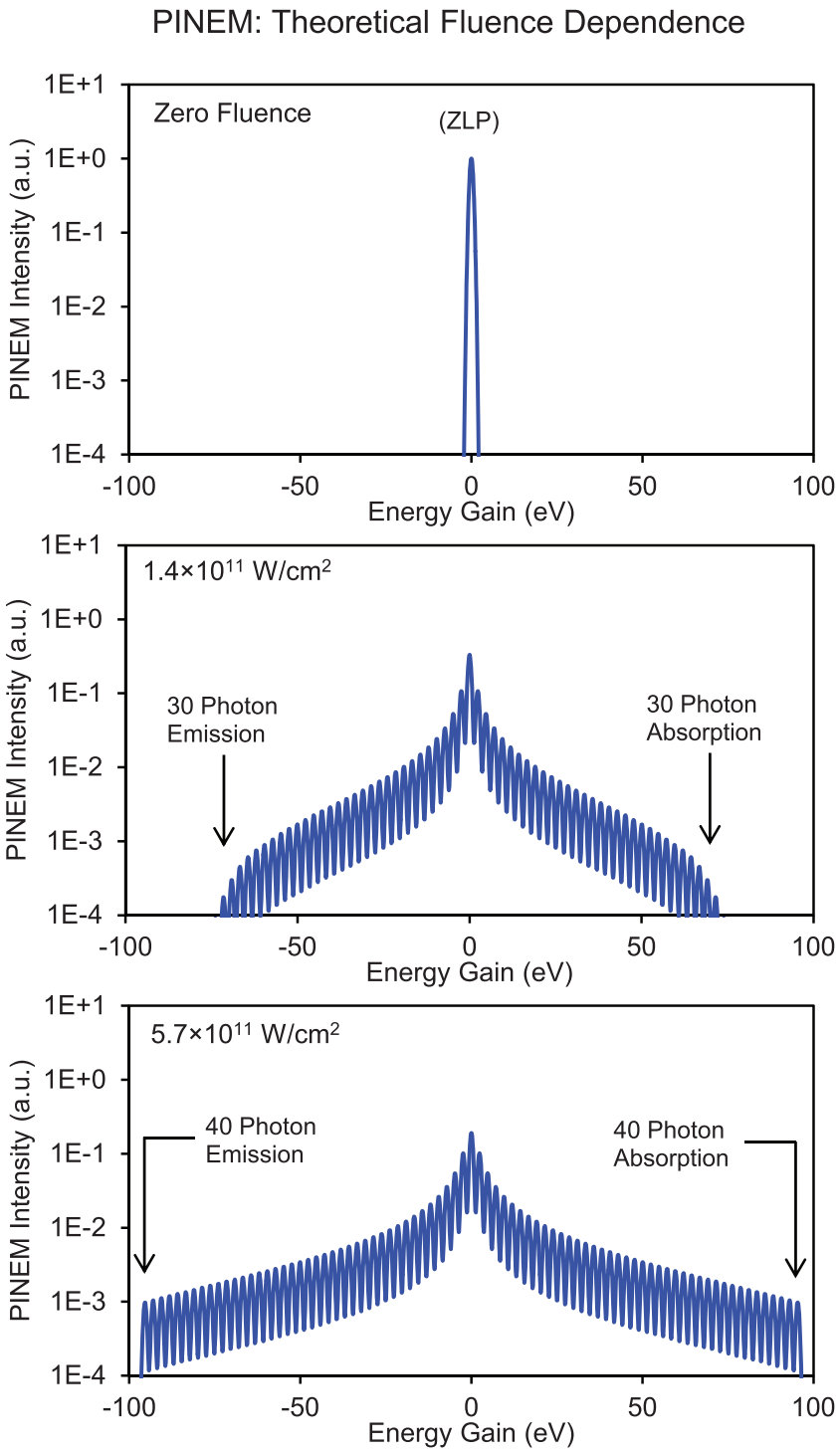

Figure 18. Theoretical dependence of PINEM on the fluence manifested in EEGS/EELS. The spectra for a single silver wire (50 nm radius) are shown. (Top) At zero fluence, (middle) $1.4 \times 10^{11}\,\mathrm{W\,cm^{-2}}$ peak power and (bottom) $5.7 \times 10^{11}\,\mathrm{W\,cm^{-2}}$ peak power. In the latter case, absorption/emission of up to 40 photons can be observed and is consistent with the experimental results.

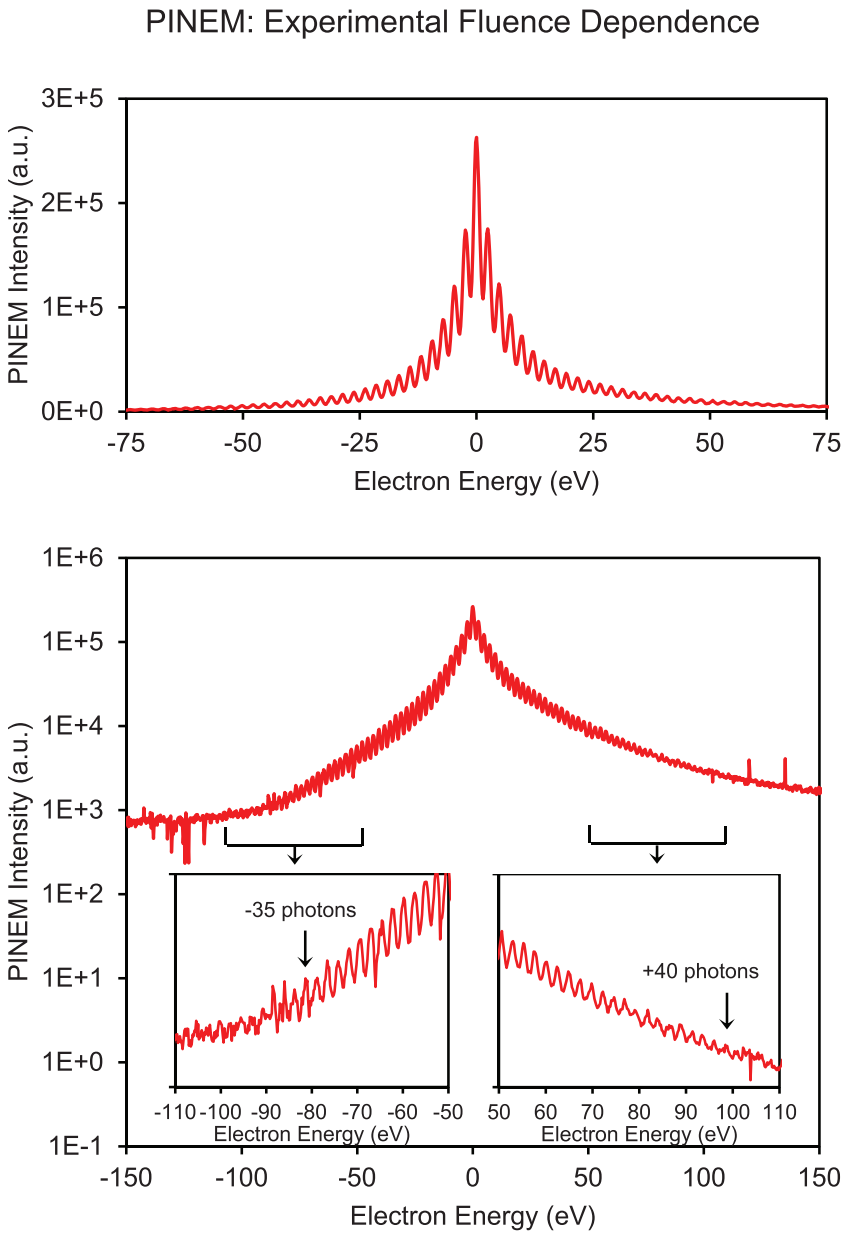

Figure 19. Experimental dependence of PINEM on the fluence manifested in EEGS/EELS. (Top) Linear and (bottom) log plots of the experimental EEGS/EELS spectrum of a silver wire bundle. Absorption/emission of up to 40 photons is observed. Data were obtained by Brett Barwick and David Flannigan of this laboratory (see text).

considering the sum over the impact parameter, b, and azimuth angle, ϕ, the incoherent-coupling model results in equation (C.13), which is similar to the coherent-coupling counterpart, equation (29). For the incoherent-coupling model, figure 16 (bottom) shows the spatially averaged electron intensity for a single silver wire at $\tau = 0$ as a function of the peak laser power; note that 10^{10} W cm^{-2} corresponds to $eF_z/\hbar\omega_p \sim 8$.

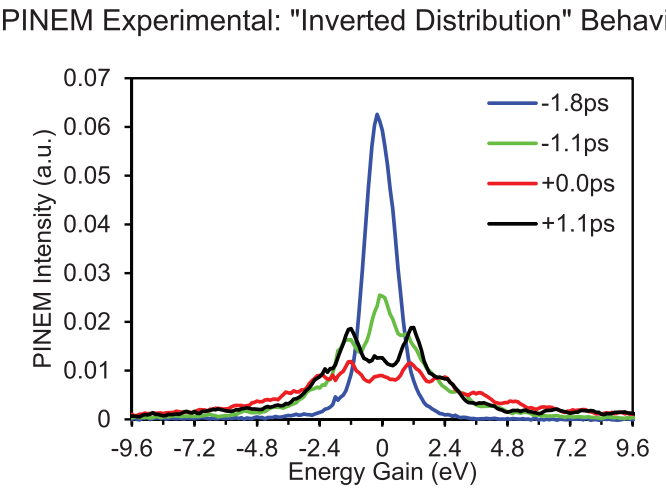

Figure 20. Experimental PINEM showing 'inverted distribution' behavior. Plot of the experimental EEGS/EELS spectrum of a silver wire bundle with 1038 nm incident light at different delays between electron and light pulses. At zero delay, the first-order peaks (absorption and emission of single photon) are more populated than others, including the zero loss peak (ZLP). This unique pattern is reproduced theoretically and is due to the fact that b-summing for a bundle of wires exhibits more of the small b-values than b-summing for a single wire (see text).

From the above discussion, it follows that the nature of electron–photon coupling in PINEM, coherent versus incoherent, may be elucidated from studies of the oscillatory behavior of the fluence dependence. However, because of summing over the impact parameter, the dependence on fluence becomes less distinct in the range examined (figure 16). We speculate that both the coherent and the incoherent formulations describe sequential interactions of the electron with single photons, rather than simultaneous multiphoton exchange that gives rise to harmonic generation; the sequential interaction also describes the inverse Cerenkov and inverse Smith–Purcell effects. In the energy profile, at high fluence and with up to 40 net photons absorbed/emitted, the oscillatory behavior may have some signature, as the results in figure 20 for silver nanotubes may suggest; further studies will be carried out for this regime.

6. Summary and outlook

In this contribution, we report theoretical and experimental studies of PINEM. Stimulated by recent experimental results [1, 2] and those reported here, we address in this paper the STS formulation that provides closed-form solution and analytical descriptions of the key parameters involved in PINEM. Manifestations of various properties are discussed, including nanostructure size, material, polarization, fluence and time dependence. The near field of the nanostructure, when its size is less than or comparable to the wavelength of radiation, is obtained within the framework of scattering theory (Rayleigh and Mie), whereas the electron interaction with this near field is derived using the time-dependent Schrödinger equation. Comparisons with the experimental results are made, and some of the key findings are summarized in the following points.

Firstly, PINEM offers several domains of study: real-space imaging, real-time dynamics and real-time energy spectra (EELS/EEGS), as well as their dependencies on polarization, fluence and wavelength of the incident radiation field. These characteristics are elucidated here by considering the phase and direction of the scattered field from the nanostructure and the solution of the time-dependent amplitudes as a result of the (quantum) interaction with pulsed electron packets. The PINEM field, as we call it, provides a physical picture of what is expected in experiments, and when this field is Fourier transformed, comparisons with the experimental results are directly made in the different domains. We also discussed the two regimes of pulsed versus CW modes of excitation.

Secondly, the striking electron absorption/emission of up to 40 photons can be understood from consideration of the energy–momentum phase matching and the nature of the scattered near field from the nanostructure. In PINEM, the energy exchange involves inelastic processes and it is possible to absorb/emit (accelerate/decelerate) net single photons ($n = 0, \pm 1, \pm 2, \ldots$). In contrast, for the KD effect, the process is elastic (absorption and stimulated emission) and transverse momentum changes give rise to a minute deflection with even quanta of momentum exchange. These considerations of energy–momentum conservation, which have their roots in the nature of interaction between electrons and the electromagnetic field ($\vec{A} \cdot \hat{p}$ versus A^2 terms of the Hamiltonian; see text), can be understood within the framework of spatial and temporal confinements as dictated by the uncertainty principle ($\Delta z \leftrightarrow \Delta p_z$ and $\Delta t \leftrightarrow \Delta E$).

Thirdly, the multiple absorption/emission of single photons in PINEM is possible because energy–momentum conservation is satisfied over a broad range of dispersion energy. The momentum conservation (velocity matching) condition is virtually unchanged after absorption of a single photon because the electron energy is five orders of magnitude larger than the change in the electron energy (i.e. the photon energy) and therefore the electron group velocity changes very little. This is not the case for a typical KD effect, where the momentum–energy conservation condition is significantly different, and the momentum spread of the interaction confinement leads to only a few photon absorption/emission events. Accordingly, the interaction of KDE needs to be provided by a focused and intense standing wave in order to induce multiple photon absorption/emission (diffractive regime) [8]. Here, we considered these coherent interactions (interferences), as well as the kinetics using an incoherent collision model.

Fourthly, because the PINEM field and its associated processes decay on a femtosecond time scale, there is a huge advantage in utilizing the pulsed mode. The orders of magnitude enhancement achieved in UEM may be appreciated when comparing with the time-averaged, CW mode of excitation. For a tightly focused CW laser (10^6 W cm^{-2}), the number of excitations on the time scale of the field is nearly four to five orders of magnitude less than that achieved in UEM using 10–100 GW cm^{-2} irradiance. Furthermore, for CW powers of about 10 W, it would be necessary for the nanostructures to dissipate the energy without significant structural damage. In UEM, typically the average power is of the order of 100 mW. Perhaps most importantly, the precise overlap of pulses in UEM allows for signal acquisition times of only a few seconds, as every electron contributes to the gain/loss signal on the time scale of the field's existence. In contrast, for CW electron spectroscopy, the signal will be overwhelmed by a background whose magnitude is conditioned by the repetition rate and other factors. Lastly, we note that the process of $\pm n\hbar\omega$ absorption/emission reported here takes place for each single-electron, timed packet. The spatial and temporal resolutions can be optimized to the nano- and femto-scales and, as shown here, the PINEM field is proportional to the cross section, the square of the radius of the structure involved. Future PINEM experiments will extend these spatial and temporal domains.

Fifthly, the fact that the PINEM effect occurs only when the scattered light interacts with the electron allows us to achieve temporal control of the electron pulse. Scattering is virtually instantaneous, and the temporal profile of the energy-exchanged electron resembles that of the shorter laser pulse. One can temporally select the portion of the electron that overlaps with the laser pulse, achieving a shorter electron pulse and suppressing electron–laser jitter; both will be discussed in a forthcoming paper. Such arrangements can be used to accurately synchronize the optical and electron pulses without interference from electronic and structural dynamics. Because of these features, these measurements provide *in situ* characterization of the temporal duration of the electron pulse, and accurate determination of the duration when the laser power density and width, and the refractive index of the material, are known. By lowering the photon energy to near the work function of the cathode producing the electron packets, it is in principle possible [44, 45] to bring the electron pulses to the sub-100 fs domain, as demonstrated experimentally by Baum and co-workers [46].

Sixthly, separation of the electron wave packet into distinct spatial frequency components can be utilized to gain new information from the image. For example, the fact that the peak of added kinetic energy by the photon separates well from the initial zero-loss peak greatly enhances the signal-to-noise ratio. This is because the standard electron transmission image has in it a background (the analogue of an optical absorption experiment), whereas the gain peak is obtained with no background (the analogue of a fluorescence experiment). Energy-selected imaging can reveal the light scattered by nanoparticles in dark field imaging, as demonstrated in this paper. Another feature is image contrast selectivity and enhancement. Since the PINEM effect is localized to the surface of nanostructures, it can be exploited to locally enhance the electron microscopy contrast of such structures. The interaction is strong enough to induce significant fractional change (and even depletion) of the zero-loss peak, hence its utility in amplitude contrast with energy-filtering in bright field imaging. The same features can be invoked to achieve improved amplitude contrast for nanostructures and interfaces even when there is no efficient light absorption or electron phase shift by the material, as is commonly the case with light element specimens and biological samples. Other possibilities include sample thickness measurement and phase-contrast imaging. The specimen thickness induces phase differences of the type $\exp[-\mathrm{i}\Delta\Delta k d]$ in the PINEM field, where $\Delta\Delta k \equiv \Delta k_{\mathrm{e}} - k_{\mathrm{p}}$, which could be utilized to accurately measure the thickness (d) in an interferometric manner. The contribution of the A^2-term in PINEM could be exploited in 'elastic imaging' for inducing phase shifts that control phase contrast in imaging, and because of the high peak power that can be achieved, the pulsed mode would enable significant shifts. We note here that the PINEM effect does not critically depend on the photon being on resonance with a transition (as in atoms and molecules); this is because it is dependent on the broad dielectric response of the material structure.

Finally, we discuss future experiments that could exploit coherence properties of PINEM. For example, apart from its use in enhancing contrast and selectivity in microscopy, as a proof of principle, one can devise a two-color electron population interference experiment using a co-propagating fundamental and its second harmonic. Single-photon absorption of the second harmonic and two-photon absorption of the fundamental would result in the same kinetic energy change for the electron. However, the phase difference for these processes can be adjusted by inserting a dielectric material 'time-plate' with different refractive indices at those wavelengths. By changing the thickness of the time-plate and fine-tuning the temporal delay between the two pulses within one optical cycle (1.7 fs for 519 nm photons), we should be able to observe

constructive and destructive interferences for peaks of different orders. Preliminary analysis (integrated over temporal packets, but not over space) indicates that energy gain and loss can be selectively controlled for the same orders, by adjusting the phase difference between the 1038 and 519 nm pulses. Such a scheme, and related ones, opens the door to future coherent control studies with PINEM.

Acknowledgments

This work was supported by the National Science Foundation and the Air Force Office of Scientific Research in the Center for Physical Biology funded by the Gordon and Betty Moore Foundation. We are indebted to Professor Archie Howie for his genuine interest in our work and for numerous stimulating discussions with AHZ. In one of the correspondences on the subject, he sent us prior to publication his independent work on the analytical analysis of the energy loss/gain processes, which will be published in a special proceeding issue honoring Professor C Colliex. We are grateful to Professor García de Abajo for sending his publications and for his interest in our work [1, 21, 22, 47], and we appreciate the helpful discussions with Professors John Spence and Harry Atwater, and Dr Eyal Feigenbaum. The experimental effort of Drs Brett Barwick and David Flannigan of this laboratory stimulated this theoretical work, and we have benefited from numerous discussions on PINEM.

Appendix A. Quantum mechanical treatment of PINEM phenomena (the scattering-of-photon/time-dependent Schrödinger equation (STS))

Here, we calculate the time evolution of the wavefunction of an electron traveling through the electromagnetic field scattered by the interaction of an incident pulsed wave with a nanoscale structure. For this problem, García de Abajo and co-workers used the quantum scattering approach, in which the electron wavefunction following the interaction is expanded in orders of scattering, with each scattering order decomposed as a linear combination of momentum eigenfunctions with unknown coefficients. The Nth-order term was related to the $(N+1)$th-order term, a single scattering event, by considering the interaction Hamiltonian and the propagation through Green's function. In this way, an inductive relation is established between the coefficients, such that they can all be calculated recursively. In contrast, we solve the time-dependent Schrödinger equation analytically, which allows for closed form solution of the coefficients. In addition, since the Schrödinger equation describes the time evolution, we obtain the electron wavefunction as a function of time, not just after the interaction. Although the electrons in current PINEM experiments travel at two-thirds the speed of light, we limit the treatment in this contribution to the nonrelativistic formalism by solving the time-dependent Schrödinger equation. In this treatment, the velocity is the actual (relativistically correct) value for the electron, whereas the momentum and kinetic energy are the nonrelativistic values that correspond to the velocity. It is to be reminded that the dispersion relation, $\partial E/\partial p = v$, holds for both nonrelativistic and relativistic cases and therefore the energy change due to a change in momentum is the same in both pictures. For example, for an electron with $E_e = 200\,\mathrm{keV}$, the relativistic factor, the velocity and the momentum are $\gamma = 1.39$, $v_e = 0.695\,c$ and $p_e = 0.967\,m_e c$, respectively. For this velocity, the nonrelativistic kinetic energy and momentum are $E_e = 124\,\mathrm{keV}$ and $p_e = 0.695\,m_e c$, respectively. The equivalence between the two formalisms will be presented elsewhere.

The Hamiltonian for an electron in an electromagnetic field is given by [48]

$$H = \frac{1}{2m_e}(\vec{p}_e - q_e\vec{A})^2 + q_e V, \tag{A.1}$$

where $q_e = -e$ is the electron charge, m_e is the electron mass, $\vec{A}$ is the vector potential and V is the scalar potential. The ponderomotive term ($\vec{A}^2$) can be ignored when the electron momentum is much larger. Choosing the Coulomb gauge ($\nabla \cdot \vec{A} = 0$) in the case of zero charge density ($V = 0$), the vector potential is given by $\vec{E} = -\partial\vec{A}/\partial t$, and the perturbation term in the Hamiltonian for an electron in a linearly polarized electromagnetic wave of a single frequency becomes, to first order in $\vec{A}$,

$$H' \approx -\frac{q_e\hbar}{2m_e\mathrm{i}}\vec{A}\cdot\vec{\nabla} - \frac{q_e\hbar}{2m_e\mathrm{i}}\vec{\nabla}\cdot\vec{A} = \mathrm{i}\frac{q_e\hbar}{m_e}\vec{A}\cdot\vec{\nabla} = \mathrm{i}\frac{q_e\hbar}{m_e}\frac{1}{2}\left(\frac{\tilde{E}}{+\mathrm{i}\omega_p} + \frac{\tilde{E}^*}{-\mathrm{i}\omega_p}\right)\cdot\vec{\nabla}, \tag{A.2}$$

where ω_p is the angular frequency of the light, and $\tilde{E}$ is the complex representation of the electric field, $\tilde{E} = \vec{E}(\vec{r}; k_p, E_0)\exp[-\mathrm{i}\omega_p t]$ for the scattered light and $\tilde{E} = \hat{x}E_0\exp[\mathrm{i}k_p z]\exp[-\mathrm{i}\omega_p t]$ for the co-propagating incident light (we ignore the magnetic interaction, because $q\vec{v}\times\vec{B}$ is always transverse, and we are only interested in the $\hat{z}$-direction that couples with $\vec{p}_e$). Electrons can interact with the near field of the light scattered by the structure and either absorb (via the $\tilde{E}$ term) or emit (via the $\tilde{E}^*$ term) photons.

For the present study, it is convenient to follow the time evolution of the electron wavefunction in the moving frame and express the one-dimensional (1D) electron wavefunction in terms of the (moving) envelope function, such that $\Psi(z,t) = g(\mathrm{z} - v_e t, t)\psi_0(z,t)$, where v_e is the group velocity of the electron packet, $g(z',t')$ is the envelope function in the moving frame, $\psi_0(z,t) = \exp[\mathrm{i}(k_e\mathrm{z} - \omega_e t)]$ is the carrier wavefunction, and k_e and ω_e are the initial nonrelativisitc spatial frequency and angular frequency of the electron, respectively, that correspond to the velocity, v_e. In this convention, z is the position in the reference (laboratory) frame and z' is the position with respect to the center of the moving electron packet. Initially, the envelope function can be chosen to be a Gaussian function,

$$g(z', t_0 \to -\infty) = \left(\frac{1}{\sqrt{2\pi}\,v_e\sigma_e}\exp\left[-\frac{z'^2}{2v_e^2\sigma_e^2}\right]\right)^{1/2},$$

for a pulsed electron packet, or a constant for a continuous current.

With this in mind, and using the time-dependent Schrödinger equation, $\mathrm{i}\hbar(\partial/\partial t)\Psi(\vec{r},t) = H\Psi(\vec{r},t)$, we obtain

$$\mathrm{i}\hbar(\dot{g}\psi_0 - v_e g'\psi_0 - \mathrm{i}\omega_e g\psi_0) = -\frac{\hbar^2}{2m_e}(g''\psi_0 + 2\mathrm{i}k_e g'\psi_0 - k_e^2 g\psi_0) + \mathrm{i}\frac{q_e\hbar}{m_e}A_z(g'\psi_0 + \mathrm{i}k_e g\psi_0), \tag{A.3}$$

where g' and g'' denote the first- and second-order spatial derivatives with respect to z (or equivalently with respect to z'), and $\dot{g}$ is the time derivative in the moving frame, i.e. $\partial g(z',t)/\partial t|_{z'=z-v_e t}$. It is to be noted that differentiation of the first argument, $z' = z - v_e t$, with respect to time is separately given as the second term on the left-hand side. The third term on the left-hand side and the third term on the right-hand side are the temporal evolution terms and cancel each other. The second terms on both sides are the group velocity propagation terms, and they also cancel each other. Since the electron has momentum in the $\hat{z}$-direction in the 1D planar

wave approximation, only the $\hat{z}$ component of the vector potential, A_z, remains. Since ψ_0 is a common factor on both sides, it can be factored out to obtain the differential equation for the envelope function to be

$$\mathrm{i}\hbar(\dot{g}) = -\frac{\hbar^2}{2m_\mathrm{e}}(g'') + \mathrm{i}\frac{q_\mathrm{e}\hbar}{m_\mathrm{e}}A_z(g' + \mathrm{i}k_\mathrm{e}g). \tag{A.4}$$

The g' term is of the order of the reciprocal of the entire wave packet (~ 1 mm) initially and the wavelength of the light ($\sim$500 nm) intermediately, while the $\mathrm{i}k_\mathrm{e}g$ term is of the order of the reciprocal of the carrier wavelength of the electron ($\sim$2.5 pm). Therefore, we can ignore the g' term. Also, the dispersion term, $-(\hbar^2/2m_\mathrm{e})(g'')$, is negligible within the time scale of the interaction ($\ll$1ps). Dividing by $\mathrm{i}\hbar$, we obtain

$$\dot{g}(z', t) \approx \mathrm{i}\frac{q_\mathrm{e}k_\mathrm{e}}{m_\mathrm{e}}A_z(z' + v_\mathrm{e}t, t)g(z', t), \tag{A.5}$$

which is a first-order ordinary differential equation in time at any position on the moving frame [36], and its solution is readily given by

$$g(z', t) = g(z', t_0)\exp\left[\int_{t_0}^{t}\mathrm{d}t'\left(\mathrm{i}\frac{q_\mathrm{e}k_\mathrm{e}}{m_\mathrm{e}}A_z(z' + v_\mathrm{e}t', t')\right)\right]. \tag{A.6}$$

By substituting the vector potential as a function of the electric field, equation (A.6) becomes

$$\begin{aligned}\frac{g(z', t)}{g(z', t_0)} &= \exp\left[\int_{t_0}^{t}\mathrm{d}t'\left(\mathrm{i}\frac{q_\mathrm{e}k_\mathrm{e}}{m_\mathrm{e}}\frac{1}{2}\left(\frac{\tilde{E}_z(z' + v_\mathrm{e}t', t')}{\mathrm{i}\omega_\mathrm{p}} - \frac{\tilde{E}_z^*(z' + v_\mathrm{e}t', t')}{\mathrm{i}\omega_\mathrm{p}}\right)\right)\right] \\ &= \exp\left[\mathrm{i}\frac{q_\mathrm{e}k_\mathrm{e}}{m_\mathrm{e}\omega_\mathrm{p}}\int_{t_0}^{t}\mathrm{d}t'\mathrm{Im}(\tilde{E}_z(z' + v_\mathrm{e}t', t'))\right].\end{aligned} \tag{A.7}$$

Accordingly, equation (A.7) gives the envelope function in terms of the time integral of the electric field experienced by the moving electron packet. When the incident wave is a propagating Gaussian pulse,

$$\tilde{E} = E_0\exp\left[-\frac{(z - c\,(t - \tau))^2}{4c^2\sigma_\mathrm{p}^2}\right]\exp[\mathrm{i}(k_\mathrm{p}z - \omega_\mathrm{p}t)],$$

where σ_p is the standard deviation (duration) of the light intensity, and τ is the time delay between the electron and light pulses, the temporal dependence of the scattered wave needs to explicitly incorporate the propagation effect. However, because the scattered wave is localized near the nanoscale material with dimension a when the duration of the incident light is relatively long compared to the transit time of the electron around the scattering center ($\sigma_\mathrm{p} \gg (a/v_\mathrm{e}) > (a/c)$), we can neglect the propagation effect, and assume that the scattered electric field varies with the amplitude of the incident light field at the center of the structure ($z \approx 0$),

$$E_0(t) \approx E_0\exp\left[-\frac{(t - \tau)^2}{4\sigma_\mathrm{p}^2}\right].$$

Therefore, the scattered electric field becomes

$$\tilde{E} \approx \vec{E}(\vec{r}; k_\mathrm{p}, E_0(t)) \exp[-\mathrm{i}\omega_\mathrm{p} t] = \vec{E}(\vec{r}; k_\mathrm{p}, E_0) \exp[-\mathrm{i}\omega_\mathrm{p} t] \exp\left[-\frac{(t-\tau)^2}{4\sigma_\mathrm{p}^2}\right],$$

where we have used the fact that the scattered field is linearly proportional to the incident wave amplitude in the exact (Mie) solution and the dipole (Rayleigh) approximation. Since the complex representation of the electric field is separable in time and space variables, equation (A.7) becomes

$$\frac{g(z', t)}{g(z', t_0)} = \exp\left[\mathrm{i}\frac{q_\mathrm{e} k_\mathrm{e}}{m_\mathrm{e}\omega_\mathrm{p}} \int_{t_0}^{t} \mathrm{d}t' \,\mathrm{Im}\left(\tilde{E}_z(z' + v_\mathrm{e} t', 0) \exp\left[-\mathrm{i}\omega_\mathrm{p} t' - \frac{(t'-\tau)^2}{4\sigma_\mathrm{p}^2}\right]\right)\right], \tag{A.8}$$

and by substituting $t' = (z'' - z'/v_\mathrm{e})$, we arrive at

$$\frac{g(z', t)}{g(z', t_0)} = \exp\left[\mathrm{i}\frac{q_\mathrm{e} k_\mathrm{e}}{m_\mathrm{e} v_\mathrm{e} \omega_\mathrm{p}} \mathrm{Im}\left(\exp\left[\mathrm{i}\omega_\mathrm{p}\frac{z'}{v_\mathrm{e}}\right] \int_{z'+v_\mathrm{e} t_0}^{z'+v_\mathrm{e} t} \mathrm{d}z'' \tilde{E}_z(z'', 0)\right.\right.$$

$$\left.\left. \times \exp\left[-\mathrm{i}\omega_p \frac{z''}{v_\mathrm{e}}\right] \exp\left[-\frac{(z''-z'-v_\mathrm{e}\tau)^2}{4v_\mathrm{e}^2\sigma_\mathrm{p}^2}\right]\right)\right]. \tag{A.9}$$

Now the time integral is expressed in terms of the spatial integral of the electric field. The Gaussian function in the integral is slowly varying, and the electric field is significant only in the vicinity of $z'' = 0$. Therefore, we can make the approximation $z'' \approx 0$ in the Gaussian factor. With $m_\mathrm{e} v_\mathrm{e} = p_\mathrm{e} = \hbar k_\mathrm{e}$, equation (A.9) becomes

$$\frac{g(z', t)}{g(z', t_0)} \approx \exp\left[\mathrm{i}\frac{q_\mathrm{e}}{\hbar\omega_\mathrm{p}} \exp\left[-\frac{(z'+v_\mathrm{e}\tau)^2}{4v_\mathrm{e}^2\sigma_\mathrm{p}^2}\right] \mathrm{Im}\left(\exp\left[\mathrm{i}\frac{\omega_\mathrm{p}}{v_\mathrm{e}} z'\right] \int_{z'+v_\mathrm{e} t_0}^{z'+v_\mathrm{e} t} \mathrm{d}z'' \tilde{E}_z\left(z'', 0\right) \exp\left[-\mathrm{i}\frac{\omega_\mathrm{p}}{v_\mathrm{e}} z''\right]\right)\right]. \tag{A.10}$$

The final envelope function at $t \to +\infty$, with $t_0 = -\infty$, becomes

$$\frac{g\,(z', +\infty)}{g\,(z', -\infty)} = \exp\left[\mathrm{i}\frac{q_\mathrm{e}}{\hbar\omega_\mathrm{p}} \exp\left[-\frac{(z'+v_\mathrm{e}\tau)^2}{4v_\mathrm{e}^2\sigma_\mathrm{p}^2}\right] \mathrm{Im}\left(\exp\left[\mathrm{i}\frac{\omega_\mathrm{p}}{v_\mathrm{e}} z'\right] \int_{-\infty}^{+\infty} \mathrm{d}z'' \tilde{E}_z\left(z'', 0\right) \exp\left[-\mathrm{i}\frac{\omega_\mathrm{p}}{v_\mathrm{e}} z''\right]\right)\right]. \tag{A.11}$$

We define the 'PINEM field' as

$$\tilde{F}_z\left(\frac{\omega_\mathrm{p}}{v_\mathrm{e}}\right) \equiv \int_{-\infty}^{+\infty} \mathrm{d}z'' \tilde{E}_z\left(z'', 0\right) \exp\left[-\mathrm{i}\left(\frac{\omega_\mathrm{p}}{v_\mathrm{e}}\right) z''\right],$$

which is the Fourier transform of the scattered electric field at the spatial frequency of $\Delta k_\mathrm{e} = \omega_\mathrm{p}/v_\mathrm{e}$, the value that corresponds to $\Delta\omega_\mathrm{e} = \omega_\mathrm{p}$ according to the dispersion relation. Therefore, the envelope function can be written as

$$\frac{g(z', +\infty)}{g(z', -\infty)} = \exp\left[\mathrm{i}\frac{q_\mathrm{e}}{\hbar\omega_\mathrm{p}} \exp\left[-\frac{(z'+v_\mathrm{e}\tau)^2}{4v_\mathrm{e}^2\sigma_\mathrm{p}^2}\right] \mathrm{Im}\left(\exp\left[\mathrm{i}\frac{\omega_\mathrm{p}}{v_\mathrm{e}} z'\right] \tilde{F}_z\left(\frac{\omega_\mathrm{p}}{v_\mathrm{e}}\right)\right)\right]. \tag{A.12}$$

From equation (A.12), we see that after the interaction, the phase of the envelope function has been modulated by a sine function with spatial frequency equal to Δk_e. The final wavefunction of the electron can now be written in terms of $g(z', t)$ and $\psi_0(z, t)$ as $\Psi(z, t \to +\infty) = g(z - v_e t, +\infty)\psi_0(z, t)$.

Now we Taylor-expand the exponential function in equation (A.12) and rewrite the Im function as the subtraction of the argument by its complex conjugate to get

$$\frac{g(z', +\infty)}{g(z', -\infty)} = \sum_{m=0}^{\infty} \frac{1}{m!} \left\{ \mathrm{i} \frac{q_e}{\hbar\omega_p} \exp\left[-\frac{(z' + v_e\tau)^2}{4v_e^2\sigma_p^2} \right] \frac{1}{2\mathrm{i}} \left(\exp\left[\mathrm{i} \frac{\omega_p}{v_e} z' \right] \tilde{F}_z - \exp\left[-\mathrm{i} \frac{\omega_p}{v_e} z' \right] \tilde{F}_z^* \right) \right\}^m$$

$$= \sum_{m=0}^{\infty} \frac{1}{m!} \left\{ \frac{q_e}{2\hbar\omega_p} \exp\left[-\frac{(z' + v_e\tau)^2}{4v_e^2\sigma_p^2} \right] \right\}^m \sum_{u+l=m} B_u^m \left\{ \exp\left[\mathrm{i} \frac{\omega_p}{v_e} z' \right] \tilde{F}_z \right\}^u \left\{ -\exp\left[-\mathrm{i} \frac{\omega_p}{v_e} z' \right] \tilde{F}_z^* \right\}^l, \tag{A.13}$$

where B_u^m is the binomial coefficient [29, 30]. By re-arranging the summation with $m = |n| + 2j$, $n = u - l$, $u = n + j$ and $l = j$, we obtain

$$\frac{g(z', +\infty)}{g(z', -\infty)} = \sum_{n=-\infty}^{\infty} \left\{ \exp\left[\mathrm{i} \frac{\omega_p}{v_e} z' \right] \right\}^n \sum_{j=0}^{\infty} \frac{1}{(|n| + 2j)!} \left\{ \frac{q_e}{2\hbar\omega_p} \exp\left[-\frac{(z' + v_e\tau)^2}{4v_e^2\sigma_p^2} \right] \right\}^{|n|+2j}$$

$$\times B_j^{|n|+2j} \{\tilde{F}_z\}^{n+j} \{-\tilde{F}_z^*\}^j. \tag{A.14}$$

Equation (A.14) reduces to

$$\frac{g(z', +\infty)}{g(z', -\infty)} \to \sum_{n=-\infty}^{\infty} \exp\left[\mathrm{i} \frac{n\omega_p}{v_e} z' \right] \left(\frac{\tilde{F}_z}{|\tilde{F}_z|} \right)^n J_n \left(\frac{q_e}{\hbar\omega_p} |\tilde{F}_z| \exp\left[-\frac{(z' + v_e\tau)^2}{4v_e^2\sigma_p^2} \right] \right), \tag{A.15}$$

where J_n is the Bessel function of the first kind [29, 30]. The same answer can be obtained using the Jacobi–Anger relation [30], $\exp[\mathrm{i}u \sin x] = \sum_{n=-\infty}^{\infty} \exp[\mathrm{i}nx] J_n(u)$. Defining the amplitude coefficients as

$$\xi_n(z') \equiv \left(\frac{\tilde{F}_z}{|\tilde{F}_z|} \right)^n J_n \left(\frac{q_e}{\hbar\omega_p} |\tilde{F}_z| \exp\left[-\frac{(z' + v_e\tau)^2}{4v_e^2\sigma_p^2} \right] \right),$$

the final wavefunction becomes

$$\Psi(z, t) = g(z - v_e t, -\infty) \sum_{n=-\infty}^{\infty} \xi_n(z - v_e t) \exp\left[\mathrm{i} \left\{ \left(k_e + n \frac{\omega_p}{v_e} \right) z - (\omega_e + n\omega_p)\, t \right\} \right]. \tag{A.16}$$

Equation (A.16) describes the final state of the electron after passing through the scattered field. From the initial momentum at $p_e = \hbar k_e$, the wavefunction evolves into a superposition of momentum distributions of $p_e = \hbar(\mathrm{k}_e + n(\omega_p/v_e))$. The energy of the electron changes by $n\hbar\omega_p$, while the momentum changes by $n(\hbar\omega_p/v_e)$, as required by the dispersion relation for the electron. $\xi_n(z')$, the amplitude of the nth component, is a function of $\tilde{F}_z(\omega_p/v_e)$, the 'PINEM field' component of the electric field at the spatial frequency of $\Delta k_e = (\omega_p/v_e)$.

Since the Bessel function is cosine-like for large arguments,

$$J_n(\Omega) \approx \sqrt{\frac{2}{\pi\Omega}}\cos\left(\Omega - \frac{n\pi}{2} - \frac{\pi}{4}\right),$$

equation (A.16) is only computationally useful when the light is continuous ($\sigma_p \to \infty$), such that the J_n terms become independent of z'. In such a case, the envelope function becomes a summation of spatial frequency components, $\exp[in(\omega_p/v_e)z']$, with the coefficient of $(\tilde{F}_z/|\tilde{F}_z|)^n J_n((q_e/\hbar\omega_p)|\tilde{F}_z|)$, whose population becomes $\{J_n((q_e/\hbar\omega_p)|\tilde{F}_z|)\}^2$. It is to be mentioned that the Fourier transform of the envelope function yields a relative spatial frequency change distribution, whereas including ψ_0 in the Fourier transformation shifts the envelope function by k_e, and the initial Gaussian envelope function will broaden each nth spatial component by $(2v_e\sigma_e)^{-1}$ for the continuous light case, where σ_e is the temporal length of the electron packet.

On the other hand, for a pulsed light source, the population distribution (especially the zero loss peak) depends on the electron pulse length, the laser duration length and the time delay between the two. If the light pulse duration is shorter than the electron packet duration, equation (A.15) cannot be analytically decomposed any further. However, for a slowly varying pulsed light source, we may use equation (A.15) to approximate the population distribution. Here, we will assume that the J_n term in equation (A.15) is the slowly varying position-dependent amplitude of $\exp[in(\omega_p/v_e)z']$ and therefore the square of the J_n term represents a local fraction of the nth state, such that we can evaluate the total fraction by averaging it over the electron envelope as

$$P(n;\tau) = \int_{-\infty}^{+\infty} \mathrm{d}z' \left| g(z',-\infty) J_n\left(\frac{q_e}{\hbar\omega_p}|\tilde{F}_z| \exp\left[-\frac{(z'+v_e\tau)^2}{4v_e^2\sigma_p^2}\right]\right)\right|^2. \tag{A.17}$$

We later confirm that the exact treatment, via Fourier transforming equation (A.12) and integrating the amplitude squared in the vicinity of the center spatial frequency of the nth state, agrees with equation (A.17).

Equation (A.17) cannot be analytically simplified and needs to be numerically integrated. However, equation (A.14) can be Fourier-transformed to yield $P(n;\tau)$ as an infinite summation of absorption/emission probabilities, as follows. With

$$g(z',-\infty) = \sqrt{\frac{1}{\sqrt{2\pi}v_e\sigma_e}}\exp\left[-\frac{z'^2}{4v_e^2\sigma_e^2}\right]$$

explicitly, we now take equation (A.14), and re-arrange the exponential terms as

$$g(z',+\infty) = g(z',-\infty)\sum_{n=-\infty}^{\infty}\sum_{j=0}^{\infty} C_j^n \exp\left[in\Delta k_e z' - \frac{(|n|+2j)(z'+v_e\tau)^2}{4v_e^2\sigma_p^2}\right]$$

$$= \sqrt{\frac{1}{\sqrt{2\pi}v_e\sigma_e}}\sum_{n=-\infty}^{\infty}\sum_{j=0}^{\infty} C_j^n \exp\left[in\Delta k_e z' - \frac{(z'+c_j^n)^2}{2(\Sigma_j^n)^2} - d_j^n\right], \tag{A.18}$$

where

$$C_j^n = \frac{B_j^{|n|+2j}}{(|n|+2j)!}\left(\frac{q_e\tilde{F}_z}{2\hbar\omega_p}\right)^{n+j}\left(-\frac{q_e\tilde{F}_z^*}{2\hbar\omega_p}\right)^{j} = \frac{1}{(|n|+j)!\,j!}\left(\frac{q_e\tilde{F}_z}{2\hbar\omega_p}\right)^{n+j}\left(-\frac{q_e\tilde{F}_z^*}{2\hbar\omega_p}\right)^{j},$$

$$c_j^n = \frac{v_e\tau(|n|+2j)\sigma_e^2}{\sigma_p^2+(|n|+2j)\,\sigma_e^2}, \quad \Sigma_j^n = \sqrt{\frac{2v_e^2\sigma_p^2\sigma_e^2}{\sigma_p^2+(|n|+2j)\,\sigma_e^2}} \text{ and } d_j^n = \frac{(|n|+2j)\,\tau^2}{4(\sigma_p^2+(|n|+2j)\,\sigma_e^2)}.$$

Equation (A.18) shows that the nth state is a summation of (un-normalized) Gaussian packets with a width of Σ_j^n and coefficients of $C_j^n \exp[-d_j^n]$, which are alternately positive and negative with respect to j. By inverse Fourier transformation into the spatial frequency space, one obtains the spatial frequency amplitude spectrum,

$$\hat{g}(k',t) = \sqrt{\frac{1}{\sqrt{2\pi}\,v_e\sigma_e}}\sum_{n=-\infty}^{\infty}\sum_{j=0}^{\infty} C_j^n \exp[-d_j^n]\Sigma_j^n \exp\left[-ic_j^n(k'-n\Delta k_e) - \frac{(k'-n\Delta k_e)^2}{2(\Sigma_j^n)^{-2}}\right]. \tag{A.19}$$

Equation (A.19) shows the spatial frequency distribution in the vicinity of $n\Delta k_e$ for each nth state as a summation over j components. We want to integrate the square of the amplitude by a group around $n\Delta k_e$ to evaluate the discrete population as

$$P(n) = \int_{(n-1/2)\Delta k_e}^{(n+1/2)\Delta k_e} dk' \,|\hat{g}(k',+\infty)|^2. \tag{A.20}$$

When $(\Sigma_j^n)^{-1}$ is not larger than the interval, Δk_e, for significantly populated j component and therefore the nth term does not overlap with the $(n+1)$th term, we can limit the summation only to the single nth component, and extend the integration range to infinite, and obtain

$$P(n) \approx \int_{-\infty}^{+\infty} d\Delta k' \left|\sqrt{\frac{1}{\sqrt{2\pi}\,v_e\sigma_e}}\sum_{j=0}^{\infty} C_j^n \exp[-d_j^n]\Sigma_j^n \exp\left[-ic_j^n\Delta k' - \frac{\Delta k'^2}{2(\Sigma_j^n)^{-2}}\right]\right|^2, \tag{A.21}$$

where $\Delta k' = k' - n\Delta k_e$. By re-substituting c_j^n, Σ_j^n and d_j^n and simplifying, we obtain

$$P(n) = \sum_{j=0}^{\infty}\sum_{k=0}^{\infty} C_j^n C_k^{n^*} \frac{1}{\sqrt{1+(n+j+k)\,(\frac{\sigma_e}{\sigma_p})^2}} \exp\left[-\frac{(n+j+k)\,(\frac{\tau}{\sigma_p})^2}{2+2\,(n+j+k)\,(\frac{\sigma_e}{\sigma_p})^2}\right]. \tag{A.22}$$

Equation (A.22) is exactly same as equation (10) in García de Abajo's work [21] with $\Delta_e = 2\sigma_e$, $\Delta_p = 2\sigma_p$, $N = n+2j$, $N' = n+2k$, and $L = n$. Now we can identify the analytical form of the coupling coefficient in [21] as

$$C_L^N = \frac{B(N,L)}{N!}\left(\frac{q_e\tilde{F}_z}{2\hbar\omega_p}\right)^{N+L/2}\left(-\frac{q_e\tilde{F}_z^*}{2\hbar\omega_p}\right)^{N-L/2}$$

from our result,

$$C_j^n = \frac{B_j^{|n|+2j}}{(|n|+2j)!}\left(\frac{q_e\tilde{F}_z}{2\hbar\omega_p}\right)^{n+j}\left(-\frac{q_e\tilde{F}_z^*}{2\hbar\omega_p}\right)^{j} = \frac{1}{(|n|+j)\,!j!}\left(\frac{q_e\tilde{F}_z}{2\hbar\omega_p}\right)^{n+j}\left(-\frac{q_e\tilde{F}_z^*}{2\hbar\omega_p}\right)^{j}.$$

It is to be noted that the definitions of indices are different for coefficients. We also find equation (A.17) to be valid by the same argument of a narrow spectrum invoked to derive equation (A.22).

In equation (A.22), the $\tilde{F}_z$ terms can be analytically integrated over b and ϕ, and the total fraction can be analytically expressed as an infinite summation,

$$P_{\mathrm{EEGS}}(n) = \sum_{j=0}^{\infty}\sum_{k=0}^{\infty} D_{jk}^n C_j^n C_k^{n^*} \frac{1}{\sqrt{1+(n+j+k)(\frac{\sigma_e}{\sigma_p})^2}} \exp\left[-\frac{(n+j+k)(\frac{\tau}{\sigma_p})^2}{2+2(n+j+k)(\frac{\sigma_e}{\sigma_p})^2}\right], \tag{A.23}$$

where

$$D_{jk}^n = \frac{\delta((2(n+j+k)a+\delta) - \exp[-\frac{2(n+j+k)(w-a)}{\delta}](2(n+j+k)w+\delta))}{2\sqrt{\pi}(n+j+k)^2(w^2-a^2)} \frac{\Gamma(\frac{1}{2}+n+j+k)}{\Gamma(1+n+j+k)},$$

for a spherical particle, assuming $F_z(b,\phi) \approx F_z(a,0)\exp[-(b-a)/\delta]\cos\phi$. For a cylindrical particle, the integration is approximated as a rectangle integration over b and y, and we obtain

$$D_{jk}^n = \frac{\delta(1-\exp[-\frac{2(n+j+k)(w-a)}{\delta}])}{2(n+j+k)(w-a)},$$

assuming $F_z(b,y) \approx F_z(a,0)\exp[-(b-a)/\delta]$.

In order to compare with previous work, we briefly consider the CW, weak interaction, limit of equation (A.17). The probability of single photon absorption/emission by electrons has been given [20] as

$$P(+\hbar\omega_p) = \left(\frac{e}{\hbar\omega_p}\right)^2 \left|\int \mathrm{d}z\, E_z(\vec{b},z)\exp\left[-\mathrm{i}\frac{\omega_p}{v_e}z\right]\right|^2, \tag{A.24}$$

where E_z is the real-valued representation of the electric field. In this limit, $(e/\hbar\omega_p)|\tilde{F}_z| \ll 1$, and equation (22) reduces to

$$P(\pm\hbar\omega_p) = \left\{J_1\left(-\frac{e}{\hbar\omega_p}|\tilde{F}_z|\right)\right\}^2 \approx \left(\frac{1}{2}\frac{e}{\hbar\omega_p}|\tilde{F}_z|\right)^2,$$

which agrees with equation (A.24).

Appendix B. Light scattering: Mie exact solutions

The electric field components (radial and angular) of the scattered wave, normalized by the incident wave amplitude, are given by the following expressions for a spherical nanostructure,

$$E_r = \mathrm{e}^{-\mathrm{i}\omega t}\cos\phi\sum_{n=1}^{\infty}\mathrm{i}^n\frac{2n+1}{n(n+1)}\mathrm{i}a_n\left\{\frac{\mathrm{d}^2P_n^1(\cos\theta)}{\mathrm{d}\theta^2}+\cot\theta\frac{\mathrm{d}P_n^1(\cos\theta)}{\mathrm{d}\theta}-\frac{P_n^1(\cos\theta)}{\sin^2\theta}\right\}\frac{h_n^1(kr)}{kr},$$

$$E_\theta = \mathrm{e}^{-\mathrm{i}\omega t}\cos\phi\sum_{n=1}^{\infty}\mathrm{i}^n\frac{2n+1}{n(n+1)}\left\{b_n\frac{P_n^1(\cos\theta)}{\sin\theta}h_n^1(kr)-\mathrm{i}a_n\frac{\mathrm{d}P_n^1(\cos\theta)}{\mathrm{d}\theta}\left(\frac{\mathrm{d}h_n^1(kr)}{\mathrm{d}kr}+\frac{h_n^1(kr)}{kr}\right)\right\},$$

$$E_\phi = -\mathrm{e}^{-\mathrm{i}\omega t}\sin\phi\sum_{n=1}^{\infty}\mathrm{i}^n\frac{2n+1}{n(n+1)}\left\{b_n\frac{\mathrm{d}P_n^1(\cos\theta)}{\mathrm{d}\theta}h_n^1(kr)-\mathrm{i}a_n\frac{P_n^1(\cos\theta)}{\sin\theta}\left(\frac{\mathrm{d}h_n^1(kr)}{\mathrm{d}kr}+\frac{h_n^1(kr)}{kr}\right)\right\}, \tag{B.1}$$

where the coefficients are

$$a_n = \frac{\psi_n'(\tilde{n}kr)\,\psi_n(kr)-\tilde{n}\psi_n(\tilde{n}kr)\,\psi_n'(kr)}{\psi_n'(\tilde{n}kr)\,\zeta_n(kr)-\tilde{n}\psi_n(\tilde{n}kr)\,\zeta_n'(kr)},$$

$\psi_n(\mathrm{z}) = zj_n(z)$, and $\zeta_n(\mathrm{z}) = zh_n^1(z)$. Here, $j_n(z)$ and $h_n^1(z)$ are spherical Bessel and Hankel functions of the first kind, respectively, and $P_l^m(z)$ is the associated Legendre polynomial. The prime denotes the differentiation with respect to the function argument.

It is to be mentioned that the radial component of the electric field of the scattered spherical wave, E_r, is often neglected in the far field since it decays faster than the angular components, E_θ, far away from the scattering source. However, in the near field, the radial component is comparable to the angular components, and needs to be explicitly considered. Near field enhancement was investigated by Messinger *et al* [49, 50]. It is to be noted that the Mie solution is exact but physically less intuitive than the (Rayleigh) dipole approximation (Equation (16)) because it is expressed in terms of an infinite summation of Legendre polynomials [29, 30] and spherical Hankel functions [29, 30], whose values depend on the sphere size, incident wavelength and refractive index. However, the Mie solution reduces to the simple (Rayleigh) dipole approximation when the particle size becomes very small.

As for the polarization dependence, both E_r and E_θ are proportional to $\cos\phi$ [33], where ϕ is the azimuth angle with respect to the polarization direction, $\hat{x}$. Since the longitudinal component (parallel to the propagation of the incident wave), E_z, is given as $E_z = E_r\cos\theta - E_\theta\sin\theta$, it is also proportional to $\cos\phi$. The Mie solution also can be applied to metals, which have complex-valued dielectric constants and therefore complex-valued refractive indices (for example, the refractive index of silver is $0.05 + 3.31\mathrm{i}$ at 519 nm incident excitation).

For an infinitely long cylinder, a similar solution is also possible [33]. The cylindrical solution for the scattered wave is expressed in terms of complex exponential and Hankel functions [29, 30]. Here, we only consider perpendicular incidence, where the light propagation ($\vec{k}$) is normal to the symmetry axis ($\hat{y}$). Defining $(\pi/2)-\phi$ as the angle of the light polarization ($\vec{E}_0$) with respect to the symmetry axis, the incident electric field perpendicular to the symmetry

axis is given as $E_\perp = E_0 \cos\phi$. The (normalized) electric field components of the scattered field are

$$\begin{aligned} E_r &= -\mathrm{e}^{-\mathrm{i}\omega t} \sum_{n=-\infty}^{+\infty} (-1)^n \mathrm{e}^{-\mathrm{i}n\theta} n a_n \frac{H_n^1(kr)}{kr} \cos\phi, \\ E_\theta &= \mathrm{i}\mathrm{e}^{-\mathrm{i}\omega t} \sum_{n=-\infty}^{+\infty} (-1)^n \mathrm{e}^{-\mathrm{i}n\theta} a_n \frac{\mathrm{d}H_n^1(kr)}{\mathrm{d}kr} \cos\phi, \\ E_y &= -\mathrm{i}\mathrm{e}^{-\mathrm{i}\omega t} \sum_{n=-\infty}^{+\infty} (-1)^n \mathrm{e}^{-\mathrm{i}n\theta} b_n \left(\frac{n^2 H_n^1(kr)}{k^2 r^2} - \frac{1}{kr} \frac{\mathrm{d}H_n^1(kr)}{\mathrm{d}kr} - \frac{\mathrm{d}^2 H_n^1(kr)}{\mathrm{d}(kr)^2} \right) \sin\phi, \end{aligned} \tag{B.2}$$

where the coefficients are

$$a_n = \frac{J_n'(\tilde{n}kr)\, J_n(kr) - \tilde{n} J_n(\tilde{n}kr)\, J_n'(kr)}{J_n'(\tilde{n}kr)\, H_n^1(kr) - \tilde{n} J_n(\tilde{n}kr)\, H_n^{1\prime}(kr)},$$

$$b_n = \frac{\tilde{n} J_n'(\tilde{n}kr)\, J_n(kr) - J_n(\tilde{n}kr)\, J_n'(kr)}{\tilde{n} J_n'(\tilde{n}kr)\, H_n^1(kr) - J_n(\tilde{n}kr)\, H_n^{1\prime}(kr)},$$

and $J_n(z)$ and $H_n^1(z)$ are (cylindrical) Bessel and Hankel functions of the first kind, respectively. Since the longitudinal component, E_z, is given as $E_z = E_r \cos\theta - E_\theta \sin\theta$, the polarization is also proportional to $\cos\phi$ (see equation (B.2)). For a finite-length cylinder, the solution becomes nontrivial due to edge effects and requires the multiple pole method.

Appendix C. The kinetics, incoherent-coupling model

Here, we present a statistical model describing multiple photon absorption/emission in terms of sequential electron–photon interactions, where the interactions are assumed to be incoherent. In the weak interaction regime (see equation (A.24)), the total number of interactions (including both absorption and emission of a single photon) is

$$\mu = P(+\hbar\omega) + P(-\hbar\omega) = 2\left(\frac{1}{2}\frac{e}{\hbar\omega}\left|\tilde{F}_z\right|\right)^2. \tag{C.1}$$

In this model, the interactions are due to incoherent 'collisions' between the electron and photons in the vicinity of scattering. Since $\mu \propto |\tilde{F}_z|^2$ is proportional to the light intensity (or photon density) in equation (C.1) and since μ should always be proportional to the photon density (i.e. the 'collision probability') assuming incoherent coupling, we can assume that equation (C.1) is valid in the strong interaction regime as well. Furthermore, equation (C.1) is insensitive to the initial state ($n = 0, \pm1, \pm2, \ldots$), and can be (approximately) applied to transitions from any state (both initial and intermediate). Therefore, equation (C.1) can be used to describe the total number of events for all the electron states in the statistical picture.

Let us define m as the number of interactions (both absorption and emission), u_m the total number of absorptions and l_m the total number of emissions, such that $m = u_m + l_m$ and the net change $n = u_m - l_m$. Table C.1 depicts the possible combinations of (u_m, l_m) for each m and n. With these definitions, $m = |n|,\ |n|+2,\ |n|+4,\ |n|+6,\ \ldots$. Assuming that the interaction is a

Table C.1. The number of absorptions and emissions for the total number of photon interactions and net photon energy exchange, (u_m, l_m). (See text for the meaning of the notation.)

	m							
n	0	1	2	3	4	5	6	7
−7								(0,7)
−6							(0,6)	
−5						(0,5)		(1,6)
−4					(0,4)		(1,5)	
−3				(0,3)		(1,4)		(2,5)
−2			(0,2)		(1,3)		(2,4)	
−1		(0,1)		(1,2)		(2,3)		(3,4)
0	(0,0)		(1,1)		(2,2)		(3,3)	
+1		(1,0)		(2,1)		(3,2)		(4,3)
+2			(2,0)		(3,1)		(4,2)	
+3				(3,0)		(4,1)		(5,2)
+4					(4,0)		(5,1)	
+5						(5,0)		(6,1)
+6							(6,0)	
+7								(7,0)

random process, the collision distribution is Poisson with mean expectation value, μ. Assuming that n follows a binomial distribution with equal probabilities of absorption and emission, we can evaluate the probability of net photon energy exchange at each position of the electron packet, $P_n(z')$, by summing over m,

$$P_n(z', \mu(z')) = \sum_{m=0}^{\infty} P(z', \mu(z'); n, m) = \sum_{m}^{\infty} P_{\mathrm{P}}(m; \mu(z')) P_{\mathrm{B}}\left(u_m; m, \frac{1}{2}\right), \tag{C.2}$$

where P_{P} is the Poisson distribution function and P_{B} is the binomial distribution function. By substituting $u_m = (m + n/2)$ and $m = n + 2j$, equation (C.2) becomes

$$P_n(z', \mu(z')) = \sum_{j=0}^{\infty} P_{\mathrm{P}}(n + 2j; \mu(z')) P_{\mathrm{B}}\left(\frac{n + |n|}{2} + j; |n| + 2j, \frac{1}{2}\right). \tag{C.3}$$

The summation in equation (C.3) can be analytically expressed as

$$P_n(z', \mu(z')) = \exp[-\mu(z')] I_n(\mu(z')), \tag{C.4}$$

where I_n is the modified Bessel function of the first kind. Equation (C.4) describes the net photon energy exchange distribution.

Since the high-energy electron passes by the nanometer scale particle within 1 fs, which is the order of the duration of the photon–electron interaction, and the pulse durations of the laser and electron are hundreds or more femtoseconds, the light intensity (i.e. photon density) used in equations (C.1) and (C.4) must be estimated at the time that the electron passes the scattered field. The normalized envelope of the electron density is given by

$$\rho(z, t) = \frac{1}{\sqrt{2\pi}\, v_{\mathrm{e}} \sigma_{\mathrm{e}}} \exp\left[-\frac{(z - v_{\mathrm{e}} t)^2}{2 (v_{\mathrm{e}} \sigma_{\mathrm{e}})^2}\right], \tag{C.5}$$

where σ_e is the standard deviation duration of the electron pulse. Similarly, the envelope function of the incident light intensity is given by

$$I(z,t) = I_0 \exp\left[-\frac{(z - c\,(t-\tau))^2}{2(c\sigma_p)^2}\right], \tag{C.6}$$

where σ_p is the standard deviation duration of the light pulse, c is the speed of light, τ is the time delay between the electron and light pulses and I_0 is the peak intensity of the light pulse. Since the light intensity is slowly varying compared to the interaction duration, the mean number of interactions according to equation (C.1) can be evaluated by using the light intensity when the light passes $z = 0$ at the time that the electron arrives at $z = 0$.

It is convenient to define a moving coordinate, $z' = z - v_e t$, to address each portion of the electron packet. Then equation (C.5) becomes

$$\rho(z') = \frac{1}{\sqrt{2\pi}\,v_e\sigma_e} \exp\left[-\frac{(z')^2}{2(v_e\sigma_e)^2}\right]. \tag{C.7}$$

Since the nanomaterial is centered at $z = 0$, the electron portion at z' arrives at $t = -z'/v_e$. The light intensity impinging the particle at this instant in time is

$$I\left(0, -\frac{z'}{v}\right) = I_0 \exp\left[-\frac{(0 - c(-\frac{z'}{v_e} - \tau))^2}{2(c\sigma_p)^2}\right] = I_0 \exp\left[-\frac{(z' + v_e\tau)^2}{2(v_e\sigma_p)^2}\right], \tag{C.8}$$

and the total number of interactions for the electron portion at z', $\mu(z')$, is

$$\mu(z') \approx \mu_0 \exp\left[-\frac{(z' + v_e\tau)^2}{2(v_e\sigma_p)^2}\right], \tag{C.9}$$

where we have taken advantage of the fact that $\mu \propto |\tilde{F}_z|^2 \propto E_0^2 \propto I$.

The fraction of electrons in the nth state is the convolution of the electron density with the n-photon collision probability, integrated over the electron packet,

$$f_n = \int_{-\infty}^{\infty} \mathrm{d}z'\, \rho(z') P_n(z', \mu(z')). \tag{C.10}$$

Equation (C.10) depends on τ, σ_p and σ_e directly, and on $|E_0|^2$ and $\vec{b}$ through equation (C.1).

Substituting equation (C.7) and the Taylor expansion of the modified Bessel function of the first kind in equations (C.3), equation (C.10) becomes

$$f_n = \int_{-\infty}^{\infty} \mathrm{d}z' \frac{1}{\sqrt{2\pi}\,v_e\sigma_e} \exp\left[-\frac{(z')^2}{2\,(v_e\sigma_e)^2}\right] \sum_{j=0}^{\infty} \frac{1}{j!}\{-\mu(z')\}^j \sum_{k=0}^{\infty} \frac{1}{k!(n+k)!}\left\{\frac{1}{2}\mu(z')\right\}^{n+2k}, \tag{C.11}$$

which, after integration, reduces to

$$f_n = \sum_{j=0}^{\infty}\sum_{k=0}^{\infty} c_{jk}^n \frac{1}{\sqrt{1 + (n+j+2k)(\frac{\sigma_e}{\sigma_p})^2}} \exp\left[-\frac{(n+j+2k)(\frac{\tau}{\sigma_p})^2}{2 + 2\,(n+j+2k)\,(\frac{\sigma_e}{\sigma_p})^2}\right], \tag{C.12}$$

where

$$c_{jk}^{n} = \frac{(-2)^{j}}{j!k!\,(n+k)!}\left(\frac{\mu\,(\tau=0,b,\phi)}{2}\right)^{n+j+2k} = \frac{(-2)^{j}}{j!k!\,(n+k)!}\left(\frac{e\left|\tilde{F}_{z}\right|(\tau=0,b,\phi)}{2\hbar\omega}\right)^{2(n+j+2k)},$$

for $\mu = 2(e|\tilde{F}_z|/2\hbar\omega)^2$ from equation (C.1). Integration of f_n over b and ϕ results in the EEGS probability,

$$P_{\mathrm{EEGS}}(n) = \sum_{j=0}^{\infty}\sum_{k=0}^{\infty} d_{jk}^{n} c_{jk}^{n} \frac{1}{\sqrt{1+(n+j+2k)\,(\frac{\sigma_e}{\sigma_p})^2}} \exp\left[-\frac{(n+j+2k)\,(\frac{\tau}{\sigma_p})^2}{2+2\,(n+j+2k)\,(\frac{\sigma_e}{\sigma_p})^2}\right], \tag{C.13}$$

where

$$d_{jk}^{n} = \frac{\delta((2(n+j+2k)a+\delta) - \exp[-\frac{2(n+j+2k)(w-a)}{\delta}](2(n+j+2k)w+\delta))}{2\sqrt{\pi}(n+j+2k)^2(w^2-a^2)} \frac{\Gamma(\frac{1}{2}+n+j+2k)}{\Gamma(1+n+j+2k)},$$

for a spherical particle, assuming $F_z(b,\phi) \approx F_z(a,0)\exp[-(\mathrm{b}-a)/\delta]\cos\phi$. For a cylindrical particle, the integration is approximated as a rectangle integration over b and y, and we obtain

$$d_{jk}^{n} = \frac{\delta(1-\exp[-\frac{2(n+j+2k)(w-a)}{\delta}])}{2\,(n+j+2k)\,(w-a)},$$

assuming $F_z(b,y) \approx F_z(a,0)\exp[-(\mathrm{b}-a)\delta]$.

Appendix D. Calculations

The calculation was performed using programs such as Mathematica [51], GNU Octave [52] and GNU bc [53]. The Mie calculation code was adapted from MATLAB [54] code of Mätzler [55].

References

[1] Barwick B, Flannigan D J and Zewail A H 2009 Photon-induced near-field electron microscopy *Nature* **462** 902–6

[2] Flannigan D J, Barwick B and Zewail A H 2010 Biological imaging with 4D ultrafast electron microscopy *Proc. Natl Acad. Sci. USA* **107** 9933–7

[3] Spence J C H 2003 *High-Resolution Electron Microscopy* (New York: Oxford University Press)

[4] Zewail A H and Thomas J M 2010 *4D Electron Microscopy: Imaging in Space and Time* (London: Imperial College Press)

[5] Zewail A H 2010 Filming the invisible in 4-D *Sci. Am.* **303** 74–81

[6] Zewail A H 2010 Four-dimensional electron microscopy *Science* **328** 187–93

[7] Kapitza P L and Dirac P A M 1933 The reflection of electrons from standing light waves *Proc. Camb. Phil. Soc.* **29** 297–300

[8] Batelaan H 2007 Colloquium: Illuminating the Kapitza–Dirac effect with electron matter optics *Rev. Mod. Phys.* **79** 929–41

[9] Letokhov V S 1966 Kapitza–Dirac effect *Sov. Phys.—Usp.* **9** 178–80

[10] Freimund D L, Aflatooni K and Batelaan H 2001 Observation of the Kapitza–Dirac effect *Nature* **413** 142–3

[11] Bucksbaum P H, Schumacher D W and Bashkansky M 1988 High-intensity Kapitza–Dirac effect *Phys. Rev. Lett.* **61** 1182–5

[12] Bartell L S, Thompson H B and Roskos R R 1965 Observation of stimulated Compton scattering of electrons by LASER beam *Phys. Rev. Lett.* **14** 851–2
[13] Vigoureu J M 1993 Non-radiative optics: interaction between electrons and near-optical fields *Pure Appl. Opt.* **2** 189–94
[14] Pantell R H 1997 Particle acceleration with lasers *Nucl. Instrum. Methods Phys. Res. A* **393** 1–5
[15] Kimura W D, Kim G H, Romea R D, Steinhauer L C, Pogorelsky I V, Kusche K P, Fernow R C, Wang X and Liu Y 1995 Laser acceleration of relativistic electrons using the inverse Cherenkov effect *Phys. Rev. Lett.* **74** 546–9
[16] Mizuno K, Pae J, Nozokido T and Furuya K 1987 Experimental evidence of the inverse Smith–Purcell effect *Nature* **328** 45–7
[17] Pantell R H and Piestrup M A 1978 Free-electron momentum modulation by means of limited interaction length with light *Appl. Phys. Lett.* **32** 781–3
[18] Boersch H, Geiger J and Stickel W 1966 Interaction of 25-keV electrons with lattice vibrations in LIF. Experimental evidence for surface modes of lattice vibration *Phys. Rev. Lett.* **17** 379–81
[19] Howie A 2009 Photon-assisted electron energy loss spectroscopy and ultrafast imaging *Microsc. Microanal.* **15** 314–22
[20] García de Abajo F J and Kociak M 2008 Electron energy-gain spectroscopy *New J. Phys.* **10** 073035
[21] García de Abajo F J, Asenjo-Garcia A and Kociak M 2010 Multiphoton absorption and emission by interaction of swift electrons with evanescent light fields *Nano Lett.* **10** 1859–63
[22] García de Abajo F J 2010 Optical excitations in electron microscopy *Rev. Mod. Phys.* **82** 209–75
[23] Jackson J D 1975 *Classical Electrodynamics* (New York: Wiley)
[24] Heald M A and Marion J B 1995 *Classical Electromagnetic Radiation* (Fort Worth, TX: Saunders)
[25] Maier S A 2007 *Plasmonics: Fundamentals and Applications* (New York: Springer)
[26] Sonnichsen C 2001 *Plasmons in Metal Nanostructures* (Göttingen: Cuvillier Verlag)
[27] Johnson P B and Christy R W 1972 Optical constants of noble metals *Phys. Rev.* B **6** 4370–9
[28] Stratton J A 1941 *Electromagnetic Theory* (New York: McGraw-Hill)
[29] Arfken G B 2005 *Mathematical Methods for Physicists* (Burlington, VT: Elsevier Academic)
[30] Abramowitz M and Stegun I A 1965 *Handbook of Mathematical Functions, with Formulas, Graphs, and Mathematical Tables* (New York: Dover)
[31] Ruppin R 1982 *Electromagnetic Surface Modes* (New York: Wiley)
[32] Link S and El-Sayed M A 2000 Shape and size dependence of radiative, non-radiative and photothermal properties of gold nanocrystals *Int. Rev. Phys. Chem.* **19** 409–53
[33] van de Hulst H C 1957 *Light Scattering by Small Particles* (New York: Wiley)
[34] Yuce C 2006 Free electron in a laser field: the nonrelativistic solution *Phys. Rev.* A **74** 062106
[35] Verschl M and Keitel C H 2005 Analytical approach to wave-packet dynamics of laser-driven particles beyond the dipole approximation *Laser Phys.* **15**(4) 529–35
[36] de Aldana J R V and Roso L 2000 Atomic-electron excitation by a local phase shift of the wave function *Phys. Rev.* A **61** 063401
[37] Lewis H R Jr and Riesenfeld W B 1969 An exact quantum theory of time-dependent harmonic oscillator and of a charged particle in a time-dependent electromagnetic field *J. Math. Phys.* **10** 1458–73
[38] Mie G 1908 Beiträge zur optik trüber medien, speziell kolloidaler metallösungen *Ann. Phys., Berlin* **25** 377–445
[39] Bohren C F and Huffman D R 1983 *Absorption and Scattering of Light by Small Particles* (New York: Wiley)
[40] Barber P W 1990 *Light Scattering by Particles: Computational Methods* (Singapore: World Scientific)
[41] Liu C, Kaiser T, Lange S and Schweiger G 1995 Structural resonances in a dielectric sphere illuminated by an evanescent wave *Opt. Commun.* **117** 521–31
[42] Inagaki T, Hamm R N, Arakawa E T and Birkhoff R D 1975 Optical property of bovine plasma albumin between 2 and 82 eV *Biopolymers* **14** 839–47
[43] Draine B T 2003 Scattering by interstellar dust grains. II. X-rays *Astrophys. J.* **598** 1026–37

[44] Gahlmann A, Park S T and Zewail A H 2008 Ultrashort electron pulses for diffraction, crystallography and microscopy: theoretical and experimental resolutions *Phys. Chem. Chem. Phys.* **10** 2894–909
[45] Siwick B J, Dwyer J R, Jordan R E and Miller R J D 2002 Ultrafast electron optics: propagation dynamics of femtosecond electron packets *J. Appl. Phys.* **92** 1643–8
[46] Aidelsburger M, Kirchner F O, Krausz F and Baum P 2010 Single-electron pulses for ultrafast diffraction *Proc. Natl Acad. Sci. USA* **107** 19714–9
[47] García de and Abajo F J 2009 Photons and electrons team up *Nature* **462** 861
[48] Glauber R J and Lewenstein M 1991 Quantum optics of dielectric media *Phys. Rev.* A **43** 467–91
[49] Messinger B J, Vonraben K U, Chang R K and Barber P W 1981 Local fields at the surface of noble-metal microspheres *Phys. Rev.* B **24** 649–57
[50] Quinten M 2001 Local fields close to the surface of nanoparticles and aggregates of nanoparticles *Appl. Phys.* B **73** 245–55
[51] Wolfram 2008 Mathematica (Champaign, IL: Wolfram Research)
[52] Eaton J W 2002 GNU Octave (Network Theory Limited)
[53] GNU 2006 GNU bc, arbitrary precision numeric processing language (http://www.gnu.org/software/bc/)
[54] MathWorks 2007 MATLAB (Natick, MA: MathWorks)
[55] Mätzler C 2002 *MATLAB Functions for Mie Scattering and Absorption Version 2* (Jena, Germany: Institut für Angewandte Physik)